Int. J. Electrochem. Sci., 3 **(2008)** 356 - 408

International Journal of ELECTROCHEMICAL SCIENCE
www.electrochemsci.org

A Review of Nanostructural Aspects of Metal Electrodeposition

Luisa Peraldo Bicelli[1], *Benedetto Bozzini*[2,*], *Claudio Mele*[2], *Lucia D'Urzo*[2]

[1] Dipartimento di Chimica, Materiali e Ingegneria Chimica "Giulio Natta", Politecnico di Milano, v. Mancinelli 7, 20131 Milano - Italy
[2] Dipartimento di Ingegneria dell'Innovazione, Università del Salento (formerly Univeristà di Lecce), v. Monteroni, I-73100 Lecce - Italy
[*]E-mail: benedetto.bozzini@unile.it

Received: 11 January 2008 / *Accepted:* 31 January 2008 / *Online published:* 20 February 2008

In this review we address the electrochemical growth of metals and alloys with nanometric structures controlling the functional properties of electrodeposited coatings and freestanding electroforms. Electrodeposition is starting to be regarded as a viable process for nanofabrication and - even though electrocrystallisation has received considerable attention from both the theoretical and experimental viewpoints - it is now worth focussing systematically on the role of processing and electrochemical engineering factors, in the tailoring of nanosized structural features. This information is currently scattered in the literature and a specific review would fill an information gap. This paper offers: (i) an overview of the tools currently avaliable for the description and in-situ and ex-situ assessment of the nanostructure of electrodeposited metals; (ii) a systematic discussion of the relationships among their nanostructure and mechanical and chemical properties; (iii) a rationalisation of the mechanisms of formation of the different types of nanoelectrodeposits; (iv) a critical presentation - ordered by chemical composition - of specific systems. An updated and comprehensive literature coverage is provided, based on over 300 papers.

Keywords: Nanocrystalline materials, metals, alloys, electrodeposition

TABLE OF CONTENTS

1. INTRODUCTION

Nanostructured materials are considered those in which the main structural dimensions vary at the nanometer scale, typical dimensions of interest are smaller than 100 nm. Nanometric features of nanocrystalline metallic systems relevant to the functional properties are: grain dimensions, regions of the material exhibiting a given orientation of the crystal lattice, atomic density gradients and zones with a different chemical composition. The different types of nanostructured materials share two main characteristics: (i) the atomic domains (grains or phases) are confined in space to submicrometric domains, (ii) a high fraction of atoms is found in interfacial regions. Zero-dimensional, two-dimensional and three-dimensional nanomaterials can be recognised. Atom clusters and clusters of atomic clusters can be considered zero-dimensional nanostructures. Single and multiple layers modulated in one or two dimensions are two-dimensional nanomaterials. Single layers can have a nanometric structuring within the layer. Nanophasic or nanocrystalline materials can be classified as three-dimensional nanostructures. Metallic systems with all these kinds of dimensionality can be obtained by electrodeposition, even though the broadest scope for applications is related to the three-dimensional ones. The importance of the nanometer scale stems from the fact that in this range of dimensions several properties achieve special values, essentially owing to confinement effects.

The material covered in this review is the electrodeposition of nanostructured metals from aqueous electrolytes. The main focus will be on isotropic nanosized systems and monolayers. Particulate composites will be mentioned only as far as the dispersoid is added in order to stabilise the nanostructure of the matrix. Only some hints will be given at nanometric multilayered systems. The topic of electrochemical atomic layer epitaxy will not be considered. Computer modelling issues have been omitted. Recent, comprehensive reviews on nanomaterials, their properties and relevant analysis methods are available [1-5].

1.1. Structure of nanocrystalline metals

Within nanostructured metals the atoms tend to relax towards a minimum free energy content from the interfacial regions (grain boundaries and grain boundary joints), where orientational transitions reside as well as non-equilibrium atomic densities and coordination numbers [6]. The present structural knowledge does not allow to distinguish between the structural nature of grain boundaries of poly- and nanocrystalline. metals. The actual nature of grain boundaries in nanocrystalline metallic materials is not yet fully assessed: some authors maintain that they are not different from those present in coarse-grained materials [7], while others suggest that they are amorphous [8].

Since at the nanometer scale the atomic fraction of interfacial atoms is comparable to that in the perfect crystalline sites, the structure of grain joints is unstable at room temperature and tends to evolve towards a more ordered state. Because the intercrystalline volume represents a region of stored excess energy with respect to the bulk of a grain, there is a significant driving force for grain growth in nanocrystalline materials. The structure of nanosized metals is thus thermodynamically unstable and prone to changes under annealing [9-11] or even at room temperature [12-15]. These changes typically

affect the density of crystalline defects, grain size, crystallographic orientation and grain boundary structure. The enthalpy release due to annealing of the nanocrystalline structure can be directly measured e.g. by DSC [16] and can be related to the variation of the intercrystalline volume fraction [17]. During the annealing of nanoelectrodeposits quasi-nucleation-growth processes have been reported to occur [18, 19]: the nanosized crystallites typically start to grow in a random manner, some of them act as nuclei and preferentially start to grow at the expense of the surrounding nanocrystalline material. Subsequently, both normal and abnormal grain growth processes can occur, depending on the composition of the starting material and the microstructural evolution during the early stages of grain growth [20-22]. Nevertheless a high degree of metastability has often been observed, rendering technical applicability feasible. HRTEM studies of nanocrystalline Cu have revealed a high stability of grain joints well-structured with facets and low-index interfacial planes [23]. Theoretical justification of the high stability of these out of equilibrium structures are available (e.g. molecular dynamics simulations of nanocrystalline Cu and Ni [24, 25]).

1.2. Functional peculiarities of nanocrystalline metals

The most outstanding properties of nanostructured metallic materials are listed in this section. A very sketchy approach is adopted here, for reasons of space and because the relevant literature coverage is quite comprehensive.

1.2.1. Mechanical properties

1.2.1.1. Plastic properties

The limited dimensions of nanocrystalline metal samples biased the study of the plastic properties towards indentation methods and hardness testing, in particular. If the grain dimension are decreased to the point where dislocation sources cannot function under the applied stress field, a marked increase in hardness is expected. The stress necessary to make a dislocation source operative is inversely proportional to the distance between the pinning points. A critical distance is the length for which the stress exceeds the flow constraint. The extrapolation of the Hall-Petch relation to nanometric grain dimensions predicts extremely hard materials. The Hall-Petch relation has been proved to hold for grain dimensions down to a few tens of nm. The material constants are somehow altered, but the -0.5 exponent is typically valid. No accord is found in the literature for <30 nm, different and contradictory trends have been reported [26]. The physical reason for the breakdown of the Hall-Petch relation is given by the critical dimension of a grain which can support the formation of a dislocation loop (Frank-Read source). For lower grain dimensions the deformation mechanism might be based on intercrystalline flow processes rather than intracrystalline dislocation movement. When the intercrystalline flow mechanism is active, a rapid decrease of the yield stress with grain dimensions is anticipated, giving rise to grain-boundary flow with possibility of low-temperature superplastic behaviour [27] and plastic behaviour of typically brittle systems, such as intermetallics [28]. A

discussion of dislocation dynamics in the relevant systems with extensive literature references is reported in [29].

Nanocrystalline materials are expected to exhibit much higher creep rates than the corresponding microcrystalline analogues because both lattice and grain boundary diffusion [30] as well as grain boundary sliding mechanisms [31] are enhanced by reduced grain dimensions. Self-diffusivity has been shown to be ca. 3 orders of magnitude higher in nanocrystalline metals than in conventional ones [32].

1.2.1.2. Wear resistance

Grain-size reduction has been shown to lead to remarkable improvements in wear resistance of nanocrystalline metals and metal-matrix composites. Most studies on the wear behaviour of nanostructured materials have focussed on dual-phase alloys and composites [33]. A limited number of systematic investigations on pure nanocrystalline metals has been reported [34, 35]. The friction behaviour of nanolamellar multilayers has been shown to be dominated by the chemical composition of the material, the nanostructure playing a minor role in both unlubricated and lubricated conditions. Under high applied stresses the wear behaviour is again dominated by the chemical composition, probably owing to mechanical mixing. For mild wear situations however the nanolamellar systems behave considerably better than the coarse-lamellar analogues or corresponding alloys. In these conditions the wear resistance correlates with system hardness in a way which can be described by the Archard law [36].

1.2.1.3. Residual stress

A potential drawback of nanocrystalline metals are high levels of internal stresses, which are generally negatively correlated with grain dimensions. When the individual nanocrystals grow, attractive forces tend to bridge the gap between them, since the interaction with the substrate or the underlying deposit hinders this approach, stress originates [37]. The coarse-grained deposits may be crack-free and stress relief can be provided by grain growth; for nanocrystalline materials the only way to release high internal stresses is by cracking.

1.2.2. Magnetic properties

Reductions in magnetocrystalline anisotropy and coercivity are obtained as grain size is reduced below the mean thickness of magnetic domain walls. Nanocrystalline ferromagnetic materials are thus expected to exhibit low coercivity. In addition grain-size reduction may have limited effects on magnetisation [38-40]. The combination of enhanced magnetic properties and high wear resistance is expected to lead to an ideal combination of properties for magnetic recording materials [41]. Metallic multilayers of nanometric thickness, alternating magnetic and non-magnetic layers, are attractive for giant magnetoresistance applications. Giant magnetoresistance has also been observed in

inhomogeneous granular films produced by electrodeposition, containing magnetic and non-magnetic nanometric phases [42].

1.2.3. Catalytic properties

The topography of real solid surfaces plays an important role in defining the electronic energy distribution at surface sites, particularly when irregularities at the atomic level are taken into account. Likewise, surface irregularities at the nanometric level determine the electrocatalytic properties. In fact, the reactivity of small metal clusters has been found to vary by orders of magnitude when the cluster size is changed by only a few atoms [43]. Furthermore, the high surface-to-volume ratio as well as the very small particle size provide nanostructured catalysts with unique properties [44]. Sonoelectrodeposited Zn powders have been employed as catalysts for the allylation of carbonyl compounds in aqueous media [45]. Modified electrodes with monoatomic metallic layers adsorbed onto metallic surfaces can display peculiar electrocatalytic effects [46].

1.2.4. Electronic properties

The large volume fraction of grain boundaries in nanocrystalline metals typically gives rise to an increased electrical resistivity [47], which might be an advantage in soft magnetic materials. Even though the resistivity of nanocrystalline Cu is higher than that of the annealed metal, this material is nevertheless very attractive also for low-resistance applications in the semiconductor industry [48].

1.3. Electrodeposition as a preparation method for nanocrystalline metallic systems

Recent investigations have highlighted electrodeposition as an attractive approach for the preparation of nanostructured materials. Electrodeposition provides a cost-effective and non-equipment-intensive method for the preparation of nanocrystalline and nanophase metallic materials (metals, alloys, compositionally modulated alloys and composites) either as coatings or as freestanding objects even in complex shapes (foils, wires, electroforms). The low processing temperature (around room temperature) minimises interdiffusion or chemical reaction. The film thickness can be accurately controlled by monitoring the consumed charge. Composition and defect chemistry can be controlled by electrical and fluid-dynamic means. Deposition rates of the order of several tents of microns per hour can be routinely achieved.

The electrochemical processing route can basically employ traditional electroplating equipment for the production of these materials, provided suitable processing procedures are applied. Electrodeposition can be used with conventional or modified electroplating baths and conditions to produce grain sizes in the range from essentially amorphous (where subsequent crystallisation annealing can lead to the required nanostructure) to micrometric. As a matter of fact, nanocrystalline materials have been manufactured for decades and their peculiar properties have been recognised and utilised in the industry before ultra-fine microstructures have generated explicit attention and scientific

and technological interest - not to say fashion - in the late eighties. Actually, nanometric electrodeposited alloys have been quoted since the thirties, e.g., among many other examples: Cu-Sn [49] and Cu-Pb [50].

The capability of single-step production and the ability to produce fully dense materials, free of extraneous porosity have been stressed for the electrochemical route [51]. The importance of full density cannot be overemphasised with regard to practical applications, since many of the peculiar properties attributed to nanostructures in the past have been proved to be actually due to artefacts of residual porosity [52].

Moreover nanoelectrodeposition has been recognised [53, 54] as a preparation method characterised by a remarkable degree of reproducibility. This property is due to the fact that the defect introduction mechanisms giving rise to the nanocrystallinity are intrinsic of the growth method, rather than built-in by a material post-treatment process. Special electrodeposition processing routes broaden the range of nanoelectrodeposited metallic systems which can be produced. (i) Pulse-plating can produce untextured deposits by enhancing the nucleation stage (ms pulses and high current densities) [55, 56]. (ii) Sonoelectrodeposition has been carried out by combining pulsed electroplating and synchronised ultrasound pulses [45, 57]. High-density fine powder was obtained, originating from the fact that the electrodeposited nuclei are expelled from the cathode surface by the high-intensity ultrasound pulse, thus impeding their growth. (iii) The grain dimensions and distribution can be influenced by organic additives, through the molecular action of adsorbed species on the electrode behaviour.

An electrochemical approach has been adopted for the production of laminar metal coatings and freestanding foils either from a single bath or by alternatively moving the growing electrode between two baths. These materials comprise an alternating sequence of two different metals. The electrodeposition of these systems can be obtained by applying a train of suitable potential or current pulses selectively and successively depositing the more and less practically noble metal. Each layer can renucleate on the previous one or grow epitaxially. The feasibility of epitaxial multilayer growth by electrodeposition has been shown in [58]; high biaxial stresses at the interfaces can develop, depending on the relevant lattice parameters. During multilayer growth from a single bath, the more noble species is deposited under mass-transport control conditions, this raises the possibility of developing morphological instabilities, nevertheless compact multilayers have been produced, suggesting that a significant degree of surface mobility of adatoms is associated with the electrodeposition process. When noble metals are employed, the periodic displacement method can be applied (e.g. Cu/Ag [59]), in which the plating of the less noble metal is interrupted to allow the more noble metal to be deposited by displacement at open circuit. It is worth observing that the spontaneous formation of multilayers often occurs in the electrodeposition of nanometric materials (e.g. Fe-Ni [60], Zn-Ni [61], Cu-Sb [62], Au-Cu [13]) owing to dynamic peculiarities of the electrokinetic process [63]. A complete description of this topic is beyond the scope of the present review. In this context we simply mean to stress the fact that these systems constitute two-dimensional nanostructured materials of remarkable functional properties (mainly wear resistance, giant magnetoresistance and corrosion resistance [64]) which have been successfully grown by electrodeposition. High values of: wear resistance (Cu/Ni [36]), tensile properties (Cu/Ag [59]), electrical and thermal conductivity (Cu/Ag

[65] and corrosion resistance (Ni-P/Sn [64]) have been reported for these systems. Nanophase metals can be grown in the pores of nanoporous ceramics (Au [66], Cu [67], Ni [68]) or polymeric (Ni [69], Co [70, 71]) membranes; the pores are thus used as templates to prepare nanometric cylinders. Metallic nanotubes can also be produced by this approach [72].

In addition to ease of fabrication nanoelectrodeposition displays special crystallographic features. Deviations from equilibrium phase structures are ubiquitous in metal electrodeposition for both coarse-grained and nanocrystalline deposits. It is expected that for nanocrystalline deposits, obtained under conditions of much higher electrode polarisation, the higher deviation from the equilibrium state might result in the further stabilisation of out-of-equilibrium crystallographic systems. Peculiarities in the development of crystalline preferred orientations are often observed in the electrodeposition on nanograined metallic systems.

Some implemented commercial applications of electrodeposited nanometals have been reported. (i) Production of thin copper foils on anodised Ti drums, used for printed circuit boards. Electrodeposited nanocrystalline Cu displays enhanced etching rates and exhibits the ability of allowing the fabrication of systems with reduced line pitch owing to the reduction of the grain size. On the other side, reduction of grain size reduces Cu electrical conductivity, optimisation of grain dimensions with respect to the required properties must be performed. Cu sheet for printed circuit boards is produced by drum electroforming with grain sizes in the range 50-100 nm. Soft magnets for transformer and motor cores are produced by drum electroforming of foil and wire [73]. (ii) Nanocrystallinity (10-100 nm) has been shown to be crucial in high-density fabrication in the semiconductor industry in order to achieve trench-filling capability [74]. (iii) Full-coverage with nanometric Zn coating of steel sheet has been achieved with high current densities 1-5 A cm^{-2} [75]. (iv) A process for the in-situ repair of nuclear steam generator tubing by electrodeposition of nanocrystalline Ni (100 nm) is currently applied. Ni is electroformed (in thicknesses of 0.5-1 mm) on the inner surface of tubes to obtain structural repair at sites damaged by corrosion or stress corrosion cracking phenomena. The limited thickness of the coating has a limited impact on the fluid-flow and heat-transfer performance of the steam generator [51]. (v) Electroformed jewels based on nanocrystalline Au-Cu alloys are produced on a pilot-plant scale. These jewels display improved mechanical properties and can be plated at lower thicknesses (0.1 mm instead of 0.2 mm) than for the current processes, thus allowing savings in Au consumption and reduced costs. Furthermore this process avoids the use of Cd in the alloy and of free cyanide in the bath [14].

2. MECHANISMS OF FORMATION OF NANOSTRUCTURED ELECTRODEPOSITS

Nucleation and growth modes of metal electrodeposits have a vital bearing on the development of nanostructures. Nanocrystallinity has been recognised to be achievable with systems characterised by low exchange current densities at overvoltage close to the end of the Tafel region, typically in the presence of unstable growth suppressors.

2.1. Formation of induction layers on extraneous cathodes

Three different growth modes can be distinguished, basically depending on the binding energy between the electroreduced metal adatom and the substrate and the crystallographic misfit between the adatom and substrate lattices (see e.g. [76]). In the case of weak adatom-substrate interaction three-dimensional clusters of the deposited metal form in the overpotential deposition range (Volmer-Weber growth mode) (Ag onto the (00.1) surface of highly oriented pyrolytic graphite [77], Cu onto amorphous carbon and onto polycrystalline Ag [78, 79]). No lattice misfit is present in this growth mode. Strong adatom-substrate interactions lead to the initial formation of two-dimensional layers of the deposited metal in the underpotential deposition (henceforward UPD) range. A large amount of systems are known giving rise to this behaviour [80, 81]. In principle, this growth mode can give rise to a lattice misfit. If a limited lattice misfit is present a layer-by-layer growth of the deposited metal takes place (Franck-van der Merwe growth mode), while three-dimensional islands of the deposited metal form on top of the UPD layer if either positive or negative lattice misfit develops (Stranski-Krastanov growth mode). Metal electrodeposition from aqueous solutions typically occurs by the Stranski-Krastanov and Volmer-Weber modes. Metal electrodeposition starts on extraneous electrodes with the formation of individual growth centres until a continuous or disperse layer is produced. It has been established experimentally that the number of nuclei increases linearly with time after the induction period and before saturation conditions are achieved. The saturation value depends on the operating conditions (mainly: overvoltage, concentration of the electroactive species, adsorption / desorption processes of inhibiting molecules and initial metallurgical state of the cathode); the deposits obtained at low current densities consist of a small number of nuclei, with increasing current density or overvoltage the number of growth centres increases and their dimensions decrease [82-85]. Analyses of potentiostatic current transients for the nucleation in the following systems, have been reported: Cu on anodised Ti [86] and AISI304 [87], Ni on Au [88], Hg on Pt [89], Cd on W [90], Hg on carbon microfibres [91], Ag on glassy carbon [92]. The galvanostatic transients following the imposition of a potentiostatic step reported in [86] show an initial impulse, an induction period with a current density minimum and eventually the nucleation and growth current density rise displaying a behaviour of the type $i \sim (t-t_o)^{1.5}$ (where t_o is the time at which the lowest current density is observed), denoting progressive nucleation and three-dimensional diffusion controlled growth. Stochastic analyses of electrical parameters during the electrodeposition of Ag [93] have been performed allowing the correlation of the statistics of the recorded time-series and nucleation processes. Such analyses can provide useful process-control-oriented information for the growth of nanoelectrodeposited materials.

Multimodal distributions of grains, with a given fraction of nanocrystalline material, can be obtained by varying the overvoltage [9, 94]. In the case of nanocrystalline electrodeposited Cu the pinhole number-density [48] or the deposit thickness necessary for full coverage [87] can in fact be reduced by increasing the current density. In addition, abnormal crystallite growth - leading to the formation of bimodal grain structures - can be suppressed by increasing the electrodeposition current density [48].

The nucleation of the induction layer can occur via formation of a UPD layer, as reported in Section 2.1.1, or without such phenomenon. For example, nucleation and growth of thin epitaxial Ni

films on Au(111), as observed by in-situ STM, occur without UPD and without discernible anion effects [95]. At the Ni deposition potential the Au(111) substrate exhibits a peculiar "herringbone" reconstruction: at low overvoltage the nucleation of Ni starts at the "elbows" of the reconstruction, followed by anisotropic growth of monolayer islands perpendicular to the double rows of the reconstruction. For multilayer coverages, a layered growth of the Ni film was observed, up to thicknesses of six layers.

2.1.1. Underpotentially deposited layers

The formation of UPD-type induction layers is usually too fast to be observed directly in STM experiments. Only by using very low metal concentrations of electroactive species can the metal monolayer be grown under diffusion control on the time-scale compatible with SPM observations. The Cu/Au(111) system has been investigated in a sulphate electrolyte [96]: highly defective islands were imaged, coexisting with areas where no atomic structures were discernible. The Au(111) substrate has been conjectured to be covered with a dilute layer of mobile Cu adatoms.

In this review we mainly focus on UPD effects relevant to subsequent three-dimensional growth and, in particular, on the role of non-ideal metal surfaces. It has been recognised that UPD phenomena have a significant bearing on three-dimensional electrocrystallisation processes [97-99]. Metal plating systems are often well removed from the ideal surfaces typically adopted for SPM researches. A specially attractive feature of SPM techniques is their ability to image non-periodic features, in view of the investigation of real electrodes. Such electrodes typically display marked structural and nanometric (1-30 nm) morphological irregularities (mono- and polyatomic steps and stepped terrace domains, islands and stacks of mono- and polyatomic terraces, pits, dislocations, grain boundaries) as well as chemical heterogeneities (adsorbates, alloy patches, cathodic passivation layers) which have a marked bearing on the electrocrystallisation processes.

The role of step dislocations on the formation of UPD layers has been investigated by STM. The investigated systems include Pb and Tl on non-ideal Ag(111) surfaces [100, 101]. Marked effects of the surface coverage degree and on the stability of UPD layers have been recognised. The formation of Pb/Ag(111) UPD monolayers occurs in three distinct potential ranges associated with voltammetric adsorption / desorption peaks, which relate to adsorbate formation at the morphologically different domains present on the non-ideal Ag(111). The typical sequence of surface phenomena corresponding to the three cathodic (adsorption) peaks (i), (ii) and (iii) in the cathodic-going scan are listed below. (i) Decoration of steps by a spatially delimited adsorbate extending laterally ca. 1-3 nm from the step edge. (ii) Three independent localised metal deposition processes: (ii-a) partial coverage of terrace domains excluding the periphery of the terraces by ca. 1-3 nm; (ii-b) complete coverage of monoatomic pits; (ii-c) no adsorption on monoatomic islands. (iii) Completion of monolayer coverage by: (iii-a) full coverage of the stepped terrace domains and (iii-b) adsorption of monoatomic islands.

A similar scheme is followed in the Tl/Ag(111) with non-ideal Ag(111), via formation of two Tl monolayers before Tl overpotential deposition [102]. Stepwise formation of UPD layers - related to the details of the single-crystal morphology of the substrate - has also been reported for Pb/Au(111)

[101], Ag onto the (00.1) plane of highly oriented pyrolytic graphite [77], Cu/Au(111) [103, 104] and Cu/Pt(111) [105]. Also nucleation in bulk Cu electrodeposits has been proved to be triggered by surface imperfections, such as kinks and steps [106]. The mechanical interaction of the AFM tip with Cu(110) and Cu(111) surfaces has been shown to enhance the electrodeposition rate by over an order of magnitude, owing to the localised production of defects or the mechanical removal of oxides, thus forming active sites for reductive adsorption of Cu [107, 108].

2.1.1.1. Coadsorption effects

Structural phase transitions of UPD monolayers as a function of applied potential are well known; their merely structural aspects are disregarded in this review, where the focus is on the effects of this phenomenon on the development of electrodeposited nanostructures. Two-dimensional phase transitions of Pb/Au(100) [101], Pb/Ag(hkl) [109] and Ag/Au(hkl) [110, 111] have been reported to act as precursors of subsequent three-dimensional growth. In some potential ranges open UPD lattice structures can be observed by STM. This seems typical of the electrochemical formation of two-dimensional phases, since no similar effects are observed in UHV, apart from cases of surface alloying. Effects of coadsorption on the structure of electrodeposited monolayers have been reported for several systems. (i) Cu/Au(111) in sulphate solution with coadsorption of sulphate [112-116]. (ii) Cu/Pt(111) in sulphuric acid [117, 118]. (iii) Cu/Pt(111) in sulphuric acid, two well defined UPD peaks are observed [118]. (iv) Ag/Au(111) where Ag exhibits packing densities which are a function of the size of the accompanying anion [119]. Cu/Au(hkl) systems in the presence of strongly coadsorbing anions, such as chloride, show peculiar superstructures, signalling a structure-influencing effect of the anions in Cu UPD behaviour [120-122]. The case of coadsorbed iodine has disclosed a variation of the iodine lattice due to the coadsorption of Ag directly bonded to the Au(111) surface [123]. Bulk Cu electrodeposition onto Cu(100) was studied in the presence of chloride [124]: the chloride adlattice has a dominant influence on the binding energy of adatoms to a step as well as on the activation energy for migration along a step edge and thereby controls the evolution of the step morphology. (v) Ag/Pt(111) in the presence of iodine shows an additional UPD peak with respect to the sulphate case, owing to the occurrence of coadsorption of Ag with iodine [125]. (vi) Bi/Au(111) forms open structures regardless of the counter-anion [126], but due to hydroxide coadsorption [127].

2.1.1.2 Surface alloying

It has been show by cyclic voltammetry that in both Pb/Ag(111) [128] and Tl/Ag(111) [102] systems certain UPD peaks tend to decrease if the sample is submitted to prolonged potentiostatic polarisation or to extensive potential cycling within the UPD range. Structural changes of the incomplete UPD layer are related to this fact. A rearrangement of the Pb and Tl UPD layers has been observed by STM [100, 114, 129], which can be explained with the exchange of every third atom of the Ag substrate with a Pb atom and a desorption of the excess Pb atoms into the solution, thus resulting in a surface alloy. Desorption of the surface alloy occurs at higher undervoltages than

desorption of the adsorbed UPD layer on the unmodified substrate. Surface alloying in the UPD range has been shown to occur also in the Au-Cd [130], Au-Cu [97, 131] and Au-Sn [98] systems. Typically nucleation occurs during the first voltammetric cycle, followed by growth of the alloy phase during subsequent cycling. Bulk metal crystallites nucleate and grow on top of the alloyed surface at overpotentials. The nucleation of Ni islands has been reported to be preceded by the formation of depressions within peculiar two-dimensional structures, indicating that Au surface atoms are displaced by Ni atoms, which subsequently act as nucleation centres for adlayer islands [132].

Metal electrodes can undergo restructuring even if polarised in the double-layer region. A kind of surface Ostwald ripening has been demostrated by STM for electrochemically grown Au columnar films [133]: surface-diffusion controlled coarsening of Au particles takes place without a measurable change in the standard deviation of the electrodeposit height.

2.1.2. Nucleation processes

The first stage of electrodeposition on an extraneous substrate is of course the formation of a thin film of the metal being deposited. The crystallographic nature, the thickness and the continuity of this layer is a function of the plating system. The formation of the first crystals during galvanostatic electrodeposition on extraneous substrates is characterised by a specific form of time-dependent overvoltage linked to the instantaneous surface concentration of adatoms through a Nernst-type relationship [134]. A critical overvoltage exists - corresponding to a given adatom supersaturation (typically of a factor in the range 4-7 [135]) - at which a new phase is formed. The crystallisation overvoltage has been shown to be anticorrelated with the current density / exchange current density ratio [85, 136]. The exchange current density is actually the main reason for grain growth, also driving the growth of larger grains at the expense of smaller ones.

The steady-state nucleation rate R can be expressed as [137]:

$$\text{Eq. (1)} \quad R=A\cdot\exp[-B/\eta^2]$$

where η is the overvoltage A and B are overvoltage-independent quantities.

The nucleation law can be written as [138]:

$$\text{Eq. (2)} \quad N=N_o\cdot[1-\exp(-Rt)]$$

where N is the surface density of nuclei and N_o is the respective saturation value. Nucleation does not occur simultaneously over the entire cathode surface and a diameter distribution for the crystallites ensues. Typically, the larger R the more homogeneous is the crystallite size distribution. A monomodal distribution of diameters is generally correlated with smoothness of the electrodeposits. Mass-transport effects can be accounted for by considering the dependence of the overvoltage on the limiting current density i_L:

Eq. (3) $\eta=(RT/nF)\cdot\ln[1-(i/i_L)]$

It can be noticed that if $i_L>>i$, $\eta\rightarrow 0$ and $N\rightarrow 0$. Often deposits obtained from simple salt solutions at $i\cong i_L$ display a small number of isolated nuclei which grow into coarse crystallites. Complexing in otherwise identical baths (e.g. addition of NH_4^+ [139] or $H_3PO_3^-$ [140-142] to $AgNO_3$ baths) can give rise to the formations of nanocrystalline deposits. A different action is related to the effect of organic additives adsorbed at the cathode surface: a film of organic additive probably covers the electrode at sufficiently negative potentials and basically gives rise to high overvoltage values causing nanocrystallinity of the induction layer [143-145]. The distribution of crystallite dimensions in the induction layer can thus be related to the operating conditions and to the nature of the substrate [146, 147].

Once a nucleus has been formed, the current flowing to the cathode causes a local deformation of the current density distribution in the vicinity of the growing centre. New nuclei are therefore expected to form only at a given distance from the initial nucleus [78, 79]. This results in a temporary drop of current efficiency, a decrease of cluster superficial density and an increase in cluster apparent surface. The screening zone thus produced has a radius r_S which can be estimated by the relation [148, 149]:

Eq. (4) $r_S=r_N\cdot\{[2(\eta_N-\eta)/(r_N\,\rho\,i)+1]^{1/2}-1\}$

where: r_N is the radius of the nucleus, η_N is the total overvoltage (inclusive of charge-transfer and mass-transport contributions) in the presence of the nucleation process, η is the total steady-state overvoltage after the nucleation process is over and ρ is the electrolyte resistivity. In the case of pure Tafel charge-transfer control the overvoltage η is given by Eq. (5):

Eq. (5) $\eta=(B/2.3)\cdot\ln(i/i_o)$

where B is the cathodic Tafel slope. In the case of mixed control the overvoltage η it is given by Eq. (3). The geometrical distribution of the crystallites in the induction layer can thus be related to the operating conditions. In the evaluation of cluster dynamics, number-densities and dimension distributions one should take into account the fact that the redissolution of electrodeposited clusters has been observed, which might create artefacts [87].

2.1.3. Sequential electrodeposition of nanostructured layers

The topics related to induction-layer formation on extraneous cathodes are relevant to the electrochemical fabrication of multilayers and compositionally modulated alloys. Compositional homogeneity within the layers and interface sharpness are the big issues. In fact, the single layers actually end up being more or less dilute mutual alloys of the two metals being deposited. The limits of the possibility of obtaining sharp boundaries by the potentiostatic and galvanostatic dual-pulse

methods have been tackled in [150]: nanometric resolution has been shown to be achievable. Laminar multilayers with thicknesses of a few tens of nm have been grown. Some of the investigated systems with relevance to nanoelectrodeposition are: Ag/Pd [151], Cu/Ag [59], Cu/Ni [58, 152-159], Co/Ag [41, 65, 160], Co/Pt [161], Ni/Ni-P with crystalline Ni and X-ray amorphous Ni-P [162], Ni-P with high and low P contents and both sublayers X-ray amorphous [163], Ni-P/Sn with crystalline Ni-P [64], Ni-P-W with high and low W contents and both sublayers X-ray amorphous [164].

Distinct and continuous, though microscopically rough, multilayers have been produced with nanometric thickness of both metallic layers (3 and 5 nm for Co-Ag [41], from 3 and 4 nm to 10 and 30 nm for Ni-P-W sublayers [164], 10 nm Ag interlayers in Cu-Ag systems [59]). When multilayers are deposited from single-bath systems, some alloying of the less noble metal generally occurs with small amounts of the more noble one: grain refinement of crystallites present within sublayers can ensue (e.g. a factor of 2 in Cu/Ag [59]). Curiously, although single X-ray amorphous Ni-P-W sublayers with alternating W contents were produced, crystalline grains ca. 5 nm in diameter can be detected by TEM in low-W layers near the interface with the previously deposited high-W layer. This unexpected phenomenon has been explained with local variations in composition of the low-W layer during the first stages of their deposition, brought about by the transition from high- to low-current density plating conditions [164].

2.2. Transition layers

In general, during metal electrodeposition of three-dimensional layers, the cross sectional morphology displays a sequence of three different regions from the substrate outwards. The first region is a typically narrow interfacial region, where nucleation and the initial growth stages take place. Typical grain dimensions in this zone are in the nanometric range [165]. In the first region it is also, to some extent, possible to achieve epitaxial growth of the deposit on single-crystalline features of the substrate (a whole single-crystal cathode or individual grains). Deposits obtained at low current densities and overvoltage from simple salt solutions on single-crystal cathodes may exhibit single-crystal structures [166, 167], a gradual transition from single-crystal to polycrystalline was observed by increasing the deposit thickness [166, 168]. Such transition can be interpreted in terms of crystalline defect formation by non-coherent nucleation [169, 170].

The second region has been denominated "transition zone" [87]. In this region the number, dimensions and shape of crystals tend to change progressively towards the third zone, in which the structure of the deposit is no longer influenced by the substrate, but depends only on the electrodeposition conditions. The transition zone thickness depends strongly on the nature of the substrate [165]. From a morphological point of view, nanoelectrodeposition requires the extension of the nucleation-dominated region into the whole deposit thickness.

2.3. Growth of three-dimensional layers

After the formation of induction and transition layers on an extraneous cathode, further electrodeposition proceeds in the same way as on a cathode of the same metal as the one being plated.

The two main steps of the growth process can be considered: (i) lateral growth and coalescence of the nuclei and (ii) outwards growth of the deposit by continuous nucleation. The former step plays a fundamental role in determining the structure of thin layers, the latter is responsible for the formation of crystal defects and granularity in the bulk of the electrodeposited layer [170]. In order to achieve nanograin formation in three-dimensions through massive nucleation and suppression of grain growth, high cathodic overvoltage, high adion surface coverage and low surface mobility are required. The requirements for three-dimensional growth of nanoelectrodeposits are related to the mechanisms and rate of formation of structural defects. Non-coherent nucleation has been proved to be a general mechanism of defect formation in electrocrystallisation: thermodynamic [169] and atomistic [170] analyses have been developed and compared with experimental results on electrodeposited Ni, Fe, Cu and Zn, the effects of additives have been taken into account and incorporated in the atomic-level treatment [171]. The crystal defects depend on the azimuthal disorientation angle θ between the nuclei. (i) If θ<ca. 8° a dislocation boundary is formed, (ii) if θ>ca. 8° a conventional grain boundary develops, (iii) if the nucleus is in a favourable condition for twinning, a twin boundary forms. The presence of dislocation boundaries was observed in the subgrains of Ni, Fe and Zn electrodeposits from acidic sulphate electrolytes, giving rise to nanometric domains (5, 10 and 25 nm, respectively) [169]. The model of non-coherent nucleation is not limited to the description of structural defects and departure from epitaxial relationships, but can also provide a framework for the interpretation of the structural effects imposed by the electrolysis conditions.

Furthermore, surface defects such as steps or screw dislocations are known to play a crucial role as nucleation centres. Their density and local arrangement have a strong influence on the crystallite structure of the deposit. Because of the ability of force microscopies to image surfaces in real space, these techniques are especially suited to study nucleation at defects and the growth of metal clusters [104]. STM and AFM can be used also at lower magnifications for in-situ studies in the mesoscopic range [106, 172, 173], also including pulse-plating problems [174]. In the case of Cu electrodeposits [175] nucleation has been shown to continue for several layers of equally sized nuclei, whereas crystallites form only when the surface concentration of nuclei exceeds a critical value. Subsequent growth proceeds in three-dimensions, nucleation is terminated and crystallites of micrometric dimensions eventually cover the surface. Control of nanodimensional growth of course implies stabilising the semilast growth stage.

Bulk Cu growth on flame-annealed polycrystalline Au has been studied by STM [176]. Electrodeposition was carried out on ca. 100 nm wide well ordered (100) microfacets. The induction period for Cu nucleation could be directly measured by imaging the transition from the UPD monolayer to the formation of clusters of diameter ca. 3 nm and 1-3 monolayers in height. Rough regions display a significantly higher nuclei density than ordered facets. On continuing the electrodeposition, the surface properties are homogenised. The problem of relating integral electrochemical properties based on current density measurements and local growth features obtained from STM data has been considered in [177]. No clear-cut conclusions can be drawn yet: in particular the difficulties in translating local stochastic characteristics into average quantities and uncertainties related to tip artefacts have been stressed.

The growth of bulk Cu onto Cu(100) in the presence of chloride was studied in [178]. Adlattices of oxidatively adsorbed chloride stabilise surface steps in the <100> direction. Electrocrystallisation of Cu under mass-transport control at low cathodic overvoltage proceeds by step flow in the <100> direction. The electrodeposition reaction is believed to occur via a combination of two concurrent processes: reduction of cuprous chloride at kink-saturated <100> steps and transport of newly reduced Cu adatoms along step edges. At more cathodic potentials chloride is partially desorbed and in correspondence kinked metal steps become frizzy and tend to adopt the <110> orientation of the substrate [179]. Preliminary work has been reported on the heteroepitaxial bulk growth of Ni onto Cu(100), showing that the process proceeds via step flow in the <110> direction [178].

The morphological effects of organic additives on three-dimensional Cu growth have been studied [103, 180]. Even though organic molecules could not be imaged, their effects can be accurately followed. 2-(N-morpholino)ethanesulphonic acid adsorbs onto defect sites (steps and kinks) and prevents Cu from nucleating on these same sites. Cu nucleates in a more random way and when an adequate coverage is reached, the crystallites merge to form a uniform layer. The overall effect of additives is believed to induce lateral two-dimensional growth as opposed to island formation in three-dimensional growth [103]. [180] studied the effects of benzotriazole and thiourea on the morphology of nanoelectrodeposited Cu. AFM images were analysed by the scaling analysis approach and correlated to three-dimensional growth mechanisms. Benzotriazole has been shown to smooth the deposit by inhibiting surface diffusion. Thiourea brings about the formation of three-dimensional islands on top of initially flat platelets, reflecting a two-stage growth mechanism. These results emphasise the close interplay between molecular functionality and topology of electrodeposits. Crystal violet has been reported to induce quasi-two-dimensional growth of thick layers, probably by inhibiting the cluster growth normal to the substrate [104].

2.3.1. Compact nanocrystalline deposits

For a given quantity of deposited metal, in general - under mixed kinetic control - the surface coarseness is positively correlated with the current density. In particular, charge-transfer controlled electrodeposition gives rise to large grains with generally well-defined crystallite shapes. This fact has been explained by the differences of i_o on the different developing crystal faces, while the Nernst potential is very similar: this can lead to the preferential growth of given crystal planes, because the growth rate chiefly depends on the orientation [181]. This behaviour breaks down in the case of even limited mass-transport contributions to kinetic control. Therefore at the onset of mixed control conditions, morphological changes are observed from the growth of large crystallites to compact micro- and nanocrystalline deposits [182].

Continuous nucleation during three-dimensional growth has a significant bearing on the crystallinity of the deposits: it has been shown in the case of Ni [29] that at pH ca. 3 continuous nucleation is inhibited and columnar layers tend to grow with typical dimensions around 300 nm. As the pH increases - up to the hydrate precipitation limit - the crystallite size is reduced -to typically a few tens of nm - and size uniformity across the thickness - some hundred μm - is preserved. For pH in

the hydrate precipitation range, the crystal size grows again. Grain refinement is, of course, a means of achieving smoother deposits. A similar effect was reported in [183]: Ni electrodeposition at pH 2 gives rise to elongated nanometric crystallites (ca 10-20 nm) with aspect ratios in the range 2-5. Smoothing correlated to grain refinement in the nanometric range was also observed with Cu [48]. Highly stressed Fe-Ni nanoelectrodeposits from additive-free acidic chloride baths display mirror-like finish [60]. An inhibitive effect on grain growth of the presence of the two species has been postulated in [61]. In the same frame of mind the growth of larger crystallites is explained for near-stoichiometric deposits.

Levelling effects in bulk growth can be achieved by the use of organic additives which can be incorporated into the deposit and can affect the crystallinity of the electrodeposited material. The experimental evidence hints at the fact that levelling takes place under conditions such that the supply of the substance causing inhibition of the cathodic growth is under diffusion control. Peaks at the surface receive larger amounts of the additive than recesses. Thus levelling is thought to be related to local differences in the surface concentration of the additive being electrochemically reduced at the cathode, leading to differences in the local electrodeposition current densities [184]. Levelling agents are thought to be strongly adsorbed at the metal surface and to be surrounded by the depositing atoms and eventually incorporated into the deposit. A model of levelling effects due to the non-reactive adsorption of organic additives has also been proposed. Organic additives have been shown by STM to be adsorbed strongly on the top of crystallites, thus inhibiting the formation of new growth centres and giving rise to growth at the edges of the crystallites [185].

Temperature effects on nanograin dimensions have been reported for Cu grown by pulse-plating. Grain dimensions tend to increase with bath temperature owing to enhanced ion supply by diffusional transport, decreased electrolyte viscosity and decreased adsorption rate of inhibitor molecules [85].

In addition to a smooth finish, compact nanocrystalline deposits can display surface protrusions with globular or cauliflower-like features. Typically the initial protrusions are ellipsoidal with semiaxes A and a. If a<<A and A is parallel to the cathode surface, a linear diffusion layer forms at the tip of the protrusion until a critical radius of curvature r_C (Eq. (6)) is exceeded, giving rise to the onset of spherical diffusion conditions [186].

$$\text{Eq. (6)} \quad r_C = \delta - a_o \cdot \exp[(i^2\, t\, v)/(n\, F\, \delta\, i_L)]$$

where δ is the diffusion layer thickness, v is the molar volume of the metal and a_o is the initial height of the protrusions. Once spherical diffusion control is operative, second-generation protrusions can develop inside the diffusion layer of the first-generation ones. Cauliflower morphologies develop under these conditions in a range of metal electrodeposits [41, 61, 94, 187, 188]. Direct morphological investigations showed that cauliflower-like features may in fact represent conglomerates of individual nanometric grains [189, 190]. Such clustering has been proved directly: by AFM observation of cauliflower features 50 nm in size and TEM resolution of 5 nm grains within them [190]; by comparing TEM carbon replicas (ca. 40 nm) with XRD Scherrer analyses (ca. 6 nm) [60]. Simultaneous presence of spherical and cauliflower growth features in otherwise smooth nanoelectrodeposited Fe-Ni layers have been imaged by TEM with carbon replicas.

2.3.2. Disperse nanocrystalline deposits

If an ellipsoidal feature is considered, spherical diffusion control takes place only around the tip of the protrusion. Deposition on the protrusion tip can occur under pure charge-transfer control (at overvoltages lower than the critical one for the growth of dendrites), while on the rest of the cathode mixed control prevails [191-193]. Some of the new nuclei can be precursors of carrot- or needle-like protrusions, depending on their crystal orientation and position with respect to other protrusions. Based on their morphology and in the case of fcc crystals, it is likely that the basis of the carrot-like outgrowth features are truncated high-Miller index planes growing under local low-overvoltage conditions [135, 194, 195]. Nanometric (7 nm) tip radii of electrodeposited Sn needles have been reported [193].

In conditions close to full diffusion control, disperse - i.e. dendritic, powdered or spongy - deposits can be obtained by the different mechanisms presented in this section. A dendrite can be defined as a protrusion growing under charge-transfer control, while electrodeposition on the rest of the cathode goes on under diffusion control [184, 196-198]. Dendrites of Cu, Cd, Pb, Sn, Ag have been reported. Dendrites develop if a critical overvoltage is exceeded and display a highly ordered structure, growing and branching in well-defined directions. The branches typically display nanometric dimensions. Dendritic growth is favoured by decreasing the concentration of the depositing ions, by increasing the concentration of the supporting electrolyte, by increasing the viscosity of the bath, by decreasing the temperature and by decreasing the stirring [199]. Powdered deposits basically represent dendritic electrodeposits which spontaneously fall apart during growth or which can be disrupted by mechanical action. All metals which can be electrodeposited exhibit a tendency to appear in the form of powders at current densities larger than a critical value [200]. It has also been observed that the product of the current density with the square root of the time for powder formation is a constant, as can be expected for a diffusion-controlled process [184]. Increasing the overvoltage leads to the formation of less dispersed powder with lower average particle size. Cu, Ag powders consisting of micrometric aggregates of nanometric crystals have been produced by electrodeposition. Electrolyte concentration, stirring rate and temperature have been shown to have the effects on powder quality which can be expected from the dendritic growth mode [201, 202]. The morphology of the powders is affected by galvanostatic or potentiostatic deposition modes: the former gives rise to less branched powders because the overvoltage decreases during the growth process [203].

Nanometric powders with a narrow diameter distribution around 100 nm can be produced by pulsed soloelectrochemical deposition [12, 45, 57, 204]. In this process, pulsed current and pulsed ultrasound are combined in such a way that metal clusters grow to small diameter on low-adhesion cathodes (such as polished Ti) and are subsequently detached by the ultrasonic wave generated on the cathode surface by exceeding the cavitation pressure for the electrolyte. Reported sonoelectrodeposited nanocrystalline metals are: Cu [12], Zn [45], Co [204]. It has been reported [45] that the sonoelectrodeposited powders tend to agglomerate by compression on the walls of the reaction vessel brought about by the acoustic streaming deriving from the growth process, the volume-to-surface ratio must therefore be maximised in cells for sonoelectrodeposition of nanometric powders.

The growth of protrusions in all directions under spherical diffusion control giving rise to branching and interweaving protrusions has been denominated spongy growth [198, 205, 206]. Typical spongy electrodeposits with nanometric grains and filaments are formed during the growth of Zn and Cd at low overvoltage under conditions of low nucleation rate. The mechanism for the development of a spongy morphology is not yet fully understood, nevertheless it seems that the initiation of spongy growth is due to the amplification of surface protrusions within the spherical diffusion layer forming around each independently growing grain. The growth of protrusions in all directions hints at the fact that the initial stages of growth occur under spherical diffusion control, whereas further growth takes place in the diffusion layer of the whole cathode.

Many technically relevant processes of electrochemical growth develop self-affine fractal surfaces rather than euclidean ones, owing to the presence of non-equilibrium conditions. Growth modes based on thermodynamics imply a local equilibrium at the growing surface and a mass transport parallel to the growing surface which is much faster than the flux of incoming particles. Growth models for phase growth far from equilibrium imply a flux of incoming particles which is much faster than the mass transport along the growing surface, such as surface diffusion or surface-tension relaxation. These models can be formulated according to a discrete, atomistic approach, such as Monte Carlo or Molecular Dynamics, (see, e.g. [207]) or by continuous motion equations (e.g. [208]). Typical continuous models comprise a roughening term - linked to the stochastic arrival of depositing particles - and a smoothing one resulting from surface diffusion and surface-tension relaxation (see, e.g. [209, 210]). Among other approaches, the dynamic scaling theory provides a framework for understanding fractal-like morphologies of electrodeposits, by allowing the estimation of parameters from images of the surfaces and to relate them to growth modes. From the analysis of surface profiles resulting from high lateral-resolution imaging procedures, such as STM and AFM images, the dynamic scaling parameters α (roughness exponent), β (growth exponent) and z (coarsening exponent) can be estimated from Equations (7-9):

$$\text{Eq. (7)} \quad \omega(L) \sim L^{\alpha}$$

$$\text{Eq. (8)} \quad \omega(L,t) \sim t^{\beta}$$

$$\text{Eq. (9)} \quad t_x \sim L^{z}$$

where: ω is the standard deviation of the interface height, L is the dimension of the surface, and t_x is the transition time such that for $t>t_x$ the surface becomes a scale-invariant self-affine fractal. Fractal quantities can also be derived from digitised micrographs (see, e.g. [211]). The different numerical values of α, β and z correspond to different growth models. The details are beyond the scope of this review, details can be gleaned from [209].

The fractal growth of electrodeposited Cu as a method for the preparation of nanometric (6-21 nm) particles has been described in [212]. Electrodeposition was carried out by imposing the cell voltage in a gel medium. The fractal growth conditions were favoured by inhibiting the convective motion of the electrolyte by use of a tetraethyl orthosilicate-based gel. The particle dimensions could be varied by changing the potential. Also in this case micrometric clusters are obtained, consisting of nanometric particles.

2.4. Pulse plating

Nanoelectrodeposition by pulse plating depends on two fundamental processes: the nucleation rate and the growth of existing grains. The favourable factors are the ones that cause a high nucleation rate (current density) and a slow grain growth (inhibiting molecules). The pulse plating parameters are the pulse length t_{on}, the time between two pulses t_{off}, the pulse height i_p and the average current density i_a, defined as:

$$\text{Eq. (10)} \quad i_a=(i_p \cdot t_{on})/(t_{on}+t_{off})$$

By varying these parameters the cathodic overvoltage, which influences the nucleation rate and the activation energy of nucleation E_n (see e.g. Eq. (11) after [85]) can be changed:

$$\text{Eq. (11)} \quad E_n \div [\eta+(a_S(M^{z+})/a_B(M^{z+}))^2]^{-1}$$

where a_S and a_B denote the electrode and bulk activities, respectively. Of course high overvoltage values lower E_n, thus favouring nucleation. At a given average current density, increases of grain dimensions have been reported with decreasing t_{off}, since long t_{off} times relate to high i_p, high overvoltage and high nucleation rate. Correspondingly, the grain size increases slightly for longer t_{on} times [85]. In the case of inhibitor-free baths (e.g. Pd [213]) larger crystallite sizes within the nanometer range are obtained for long t_{off}. During electrodeposition by pulse plating in the presence of organic additives (e.g. Cu with citrate [85]), metal ions generally migrate faster than the bulky organic additive molecules, therefore the metal ions are discharged first and then the inhibitor molecules occupy the active sites. In a short t_{off} time a decreased number of inhibitor molecules reach the active growth sites, before the growth continues at the next pulse. Various types of pulse plating programs are adopted in order to electrodeposit compact layers and to prevent or delay the formation of spongy or dendritic deposits [214-216]. This is particularly true for systems in which low-overvoltage conditions give rise to spongy growth and high-overvoltage ones to the development of dendrites. The rationale under morphological control by pulse plating is that outgrowth features tend to dissolve preferentially during the off or anodic period than the flat regions, thus giving rise to a smoothing process. The smoothing effect of pulse plating in particular causes spongy filaments and dendrites to be partially or completely dissolved. This means that both branching of dendrites and formation of agglomerates can be prevented and powder-like particles can be thereby obtained (Ag [217], Cu [218]); these particles are actually micrometric aggregates of nanoparticles.

As far as the deposition of smooth films is concerned, it can be observed that in galvanostatic pulse plating, for a given current density, higher overvoltage values are obtained than in steady-state conditions. Therefore, according to Eq. (1), higher nucleation rates are achieved in the induction layer and smaller grain sizes in the thick-layer growth. On the other hand, the possibility of using transient values of higher-amplitude current density leads to an increase of the ohmic drop which, according to Eq. (4), is related to smaller screening zones and therefore higher nucleation densities, higher surface coverages and lower porosity [215]. Therefore pulse plating strategies are of perspective interest for

the tayloring of nanoelectrodeposits, even though they have never been used explicitly for this purpose. By increasing the pulsating frequencies smaller crystallites can be obtained, in particular the aggregate dimensions tend to be reduced and nanometric crystallites develop [219]. An interesting point in pulse plating is that grain sizes obtained in the mixed-control range are almost as regular as those obtained in the charge-transfer control range [182]. Pulse plating has been shown to favour the growth of equiaxed nanograins [220, 221].

2.5. Role of organic additives in nanoelectrodeposition

A key issue for the formation of nanometric grains is increasing the rate of nuclei formation and reducing the crystallite growth. The latter effect can be obtained by means of complex formers for the metallic electroactive species and cathodic inhibitors being adsorbed onto the growing surface. Important for adsorption are the number of free electron pairs, the number of hydrophilic groups and the size of inhibitor molecules.

The deposits obtained in the presence of finite coverages of adsorbed species have a less perfect structure than those grown from pure electrolytes. A finer microstructure is observed and the average size of the domains giving rise to coherent diffraction is smaller. Moreover, the dislocation density is higher and, in some cases, the growth twin and stacking fault densities are higher as well [171].

While it is clear that additives must be active in limiting the growth of grains during electrocrystallisation, it has not been clear to what extent this results in segregation of species - either to grain boundaries or within the grains - in the final deposit. Markedly higher contents of C, N, H and O has been reported for nanoelectrodeposited Cu from baths containing high concentrations of citrate in comparison with microcrystalline electrodeposited Cu [85]. Ultra-high lateral resolution TOF-MS analyses combined with PIXE have been performed of nanocrystalline Ni (17 nm) electrodeposited from a saccharine-containing bath, produced by pulse plating [222]. The analysis shows ca. 0.1 at% of S contamination, uniformly distributed within the nanometric grain and not segregated to the grain boundary. Instead, C and S were noticed both at grain boundaries and in the bulk of nanoelectrodeposited Ni-P (4.3 at% P) after heat treatment (523 K, 1 h); higher (a factor of 2) concentrations were found at the grain boundary (0.1 and 0.2 at% for C and S, respectively). C and S incorporation has been found also in Ni nanoelectrodeposits from baths containing saccharine [189]. The stress-relief effect of additives has been interpreted in the framework of the coalescence theory of stress generation [37] as due to the incorporation in gaps between crystallites reducing the displacement stress [187]. Pulse plating has been reported to reduce the incorporation of extraneous material [223]. Incorporation of organic materials from citrate baths has been reported to give rise to the increase in lattice parameters of electrodeposited Cu-Fe nanograined two-phase alloys [42]. Compositional analyses by ICP-MS show the presence of impurities deriving from the electrolyte, such as ca. 550 ppm B from boric acid and interstitial C (ca. 0.9 w%), N (ca. 0.2 w%) and H (ca. 0.1 w%).

It has been known for a long time that the grain size of electrodeposited Ni can be reduced to nanometric dimensions by use of coumarin and saccharin [29, 224]. The adsorbed species interfere with the surface diffusion of adatoms and can reduce the grain size without developing internal stresses and deposit cracking. These additives introduce carbonaceous material or sulphur into the electrodeposits. Sulphur acts as solid solution strengthener and also causes intergranular embrittlement. An increase in citric acid concentration has been reported to decrease cracking in nanocrystalline Ni-W [225]. Optimal thiourea concentration can stabilise a nanocrystalline growth structure for Cu v a columnar one [87]. A range of organic species (citric acid, EDTA, malonic acid, tartaric acid) has been studied for the nanoelectrodeposition of Cu by pulse plating [85]. In particular, the effects of citric acid have been investigated and the decrease of crystallite size with increase of citric acid concentration proved. Micro-Raman spectroscopy has been used for the detection and analysis of organic species incorporated into nanocrystalline Au electrodeposits [226]. Additives are generally used to obtain smooth and compact Sn deposits. Nevertheless suitable mixtures of organic (such as ethoxylated surfactants) and inorganic (Pb^{2+}) additives can also be used for the controlled deposition of needle-like Sn features [193].

3. METHODS FOR THE STUDY OF NANOELECTRODEPOSITS AND RELATED PREPARATION PROCESSES

In this section we provide an alphabetical list of experimental methods which have been reported in the literature for the investigation of nanoelectrodeposits and nanoelectrodeposition systems. These methods encompass microscopy (electron microscopies and scanning-probe techniques), spectroscopy (atomic adsorption, characteristic X-rays, mass, Mössbauer, photoelectron, visible), diffractometry (electrons and X-rays), calorimetry, magnetometry and mechanical measurements (bending, indentations, stress, tensile testing, wear resistance).

Atomic absorption spectroscopy (AAS) has been employed for compositional analyses of alloys [188, 216, 227].

Bending test measurements has been used for the ranking of the ductility of nanoelectrodeposited layers [228].

Characteristic X-rays spectroscopy (EDX) has been employed for compositional analyses of alloys [40, 51, 60, 61, 187, 225, 229], for the evaluation of particulate content in composites [230] and for obtaining overall information on multilayers with nanometric thickness of the sublayers [164]. The line-scanning mode on cross-sections was used to check the alloy composition constancy along the thickness of the layers [60]. The mapping of sulphur incorporated from organic additives has been carried out by EDX [231]. EDX mapping of W in compositionally graded nanocrystalline Ni-W electrodeposits has been reported [232]. Possible artefacts related to electrodeposition-induced morphologies have been pointed out in [233].

Differential scanning calorimetry (DSC) has been applied for the evaluation of the thermal stability of nanograined electrdeposits [17, 234]. The repeated scan method proves useful to assess the degree of annealing of the nanostructure. The activation energy for the grain growth process was

estimated by imposing multiple heating rates. The modulated-DSC technique, in which a small sinusoidal temperature signal is superimposed to the temperature ramp, was used for the improvement of the signal-to-noise ratio [234].

Differential thermal analysis (DTA) was adopted for the study of the crystallisation behaviour [225].

Extended X-ray absorption fine structure (EXAFS) has been employed for the study of nanometer-sized structures in nanocrystalline electrodeposited alloys [235].

Field-emission scanning electron microscopy (FE-SEM) has been applied for the metallographic observation of nanocrystals in-plane [48, 236] and on cross-sections [51, 236].

High-resolution transmission electron microscopy (HRTEM) has been used for the analysis of the nanocrystallisation of X-ray amorphous electrodeposits [225] and for the characterisation of sonoelectrodeposited powders [12] and of multilayers [41].

Inductively coupled plasma optical emission spectrometry (ICP-OES) has been adopted for the chemical analysis of electrodeposited Ni from solutions containing organic thio-compounds [237].

Indentation techniques have been employed for the evaluation of some mechanical properties of nanoelectrodeposits. The use of different indentation methods has been reported: (i) microindentation (Knoop and Vickers) [9, 29, 35, 60, 61, 187, 216, 225, 228-230, 236-240], (ii) recording-hardness measurements [241], (iii) instrumented nanoindentation [183]. The last technique was also used for the characterisation of multilayered electrodeposits with the Vickers pyramid applied perpendicularly to the layer orientation [150].

Infrared absorption spectroscopy has been used to measure the total sulphur and carbon contents of nanocrystalline Ni electrodeposits [231].

Mass spectrometry - (i) Inductively coupled plasma mass spectrometry (ICP-MS) has been used [56, 236] for the analysis of impurities deriving from bath components such as organic additives and buffers. (ii) Time-of-flight mass spectrometry (TOF-MS). A three-dimensional atom probe has been developed for compositional analyses of nanomaterials with near atomic resolution [222, 240]: the position and atomic identity can be measured within a volume of typically $20\times20\times100$ nm^3. A needle-shaped specimen is used and the electric field at the apex is raised to a level at which individual surface atoms are removed by field evaporation. The resulting atoms are ionised and analysed by a position-sensitive detector. Atomic-lattice resolution can be achieved with this method. (iii) MS coupled to thermal desorption has been used to assess the nature of incorporated extraneous material in nanoelectrodeposited Au [233].

Mössbauer spectroscopy has been used for the analysis of samples containing variable amounts of Fe nanocrystals in a Cu matrix [42].

Optical microscopy (OM) has been employed for in-situ monitoring of fractal growth [212] and surface and cross-sectional observations [60, 187, 227]. Optical micrographs of cross-sections were also used for the estimation of deposition rates [60]. Cross-sectional cracking was examined in [41, 60, 187].

Perturbed $\gamma\gamma$-angular correlation spectroscopy (PAC) was used to investigate structural inhomegeneities of electrodeposited nanocrystalline alloys containing one magnetic component [242].

Positron lifetime measurements have been applied for the evaluation of voids and cavities, mainly located at grain boundaries of nanocrystalline Ni electrodeposits [237].

Proton-induced X-ray emission (PIXE) has been adopted in conjunction with TOF-MS for ultra-high lateral resolution analysis of nanocrystalline Ni [222].

Scanning electron microscopy (SEM) analyses have been reported of the in-plane morphology of nanoelectrodeposits [9, 61, 87, 94, 188, 216, 227, 229, 230, 236, 239]. Specific image-analysis procedures have been developed for the quantification of the grain dimensions from SEM images of electrodeposited metals [243] and composite [244]. Fracture surfaces of electrodeposited alloys [60, 245] and nanocomposites [239] as well as Taber-abraded samples [35] have also been examined by SEM.

Scanning-probe microscopy - Local-probe methods such as scanning tunnelling microscopy (STM) and atomic force microscopy (AFM) have been applied for the characterisation of thermodynamic, structural and kinetic aspects of electrochemical interfaces. The salient feature of these techniques is their ability to image electrode surfaces in real-space with atomic resolution. Moreover, the tip of the scanning probe can be used for the preparation of nanometric features or for electrode modifications in this scale. Well defined substrate surfaces are not required for this approach and local experiments can be carried out on realistic substrate surfaces. Well characterised electrode surfaces can of course be used for studies of model electrodeposition systems. By applying appropriate electrical programs to the tip of the STM, local electrodeposition can be induced, allowing nanopatterning; this topic - which is specific of nanotechnologies rather than nanocrystalline growth - will not be dealt with in this review, details can be found in [104, 246]. Analysis of in-plane mesoscopic morphology has also been reported [9, 48, 94, 247]. STM can be conveniently used for direct evaluation of grain size distribution [85].

Selected area electron diffraction (SAED) has been used for the discrimination of metallic nanometric phases observed by TEM from oxides or amorphous phases [35, 212, 248]. Moreover this method has been applied for the assessment of the crystallographic texture [9, 225] and for the verification of the single-phase nature (hcp v fcc) of Co [234] and Ni-P [40] nanoelectrodeposits. The nanocrystallisation of initially X-ray amorphous electrodeposits has been followed by SAED [225]. Twinning and subgrain disorientation angles were studied by SAED [169]. SAED measurements could also be carried out without thinning pretreatments by directly plating onto carbon-coated Cu TEM grids [97].

Small-angle neutron scattering was adopted for the measurement of the characteristic dimensions of regions in which the magnetic moments are misaligned coherently in nanocrystalline electrodeposited Ni [249].

Small-angle X-ray scattering (SAXS) was used for the measurement of the dimension distribution of nanometric clusters [225, 250] and of other local structures in the dimension range 1-100 nm [235].

Stress-measurements have been applied for in-situ monitoring of growth stresses. Flexible-beam [41, 60, 187, 188] and spiral contractometer [216, 251] methods have been reported.

Superconductive quantum interference device (SQUID) magnetometry has been used for the measurement of the magnetisation of samples containing small amount of ferromagnetic material [42, 252].

Surface enhanced Raman spectroscopy (SERS) has been used for the detection and analysis of contaminants incorporated into nanoelectrodeposits [226] and for the study of the interfacial behaviour of organic additives [99, 253, 254].

Tensile testing of nanoelectrodeposited foils has been carried out with low-capacity load cells for the measurement of some static (Young modulus, yield stress, ultimate tensile strength) [29, 59, 228, 239, 241, 255], dynamic (strain-rate sensitivity, work hardening) mechanical properties [237, 255] and creep [255, 256].

Transmission electron microscopy (TEM) has been applied in both the dark- and bright-field modes. Dark-field micrographs have been used for determination of nanometric features by inspection [17, 94, 165, 212, 228, 229, 230, 239, 248]. Bright- [169, 216] and bright and dark-field [35, 40, 183, 222, 225, 231, 234] micrographs were employed for the same purpose. Grain-size distribution was also estimated from TEM images [216]. Bright-field images are preferred if high degrees of lattice distorsions are encountered in nanocrystalline electrodeposits, because blurred diffraction contrast can result in an underestimate of the grain sizes by dark-field images [237]. Change of grain dimensions during sample preparation is of course critical and low-temperature thinning processes have been developed. Grain distribution was evaluated by image analysis of TEM micrographs [35, 85, 183, 234, 237]. TEM observations of electrodeposited Cu nuclei were also carried out on extremely thin (electron-transparent) amorphous carbon and Ag films without thinning pretreatments [79]. The carbon-replica method has also been employed for both planar and cross-sectional studies of extremely brittle Fe-Ni nanoelectrodeposits [41, 60, 187]. Annealing by exposure to the electron beam in the TEM was used to study the thermal stability of nanoelectrodeposits [229].

Vibrating sample magnetometry was used for the measurement of coercivity and loop squareness in magnetic deposits [40, 227]

Visible spectroscopy was employed for the quantitative determination of the composition of alloy deposits [216, 227].

X-ray diffraction (XRD) line broadening analysis was used to estimate of average grain size by the Scherrer method [10, 17, 35, 40, 61, 70, 94, 97, 188, 227, 229, 230, 232, 236, 238, 239, 255]. Corrections for instrumental line broadening were applied in [60, 183, 187, 216]. [234] analysed the (00.2) reflection of strongly textured Co. [225, 228] used the broadening of the Ni(111) line for the analysis of Ni-W alloys. Peak-broadening effects related to microstress can be accounted for and corrected dimensional (grain size and grain size distribution) information extracted [10, 12, 85, 216, 251]. Texture analysis of nanocrystalline Zn has been carried out by XRD [236]. Synchrotron XRD has been used [56, 257] for real-time analysis of nanocrystallite growth. Appropriate data analysis allows the separation of grain-dimension and strain peak broadening contributions and the evaluation of grain-size distribution. The development of preferred orientations is ubiquitous in electrodeposition and relevant observations are reported in most of the discussions of diffractograms. Texture analysis by XRD has been reported. The structural effects of the electrodeposition bath and operating

conditions and the evolution of the nanostructure brought about by annealing [9, 94, 238] have been studied.

X-ray photoelectron spectroscopy (XPS) was used for the detection of incorporated organic species [97, 188].

Wear testing of nanoelectrodeposits has been carried out by the following methods: Taber [35, 258], pin-on-disk [259], slider on cylinder [260] and nanoscratching with a load ramp [183].

4. OVERVIEW OF NANOELECTRODEPOSITED METALS AND ALLOYS

In this section we report a selection of nanoelectrodeposited metallic systems. The material is arranged alphabetically, the pure metals and the corresponding alloys are listed successively. Within each system very sober information is given concerning: bath composition and operating conditions, structure, mechanical properties and other functional properties. For details, reference is of course made to the original literature.

4.1. Au

Cyanocomplex Au(I) baths containing citrates have been studied, galvanostatic electrodeposition has been adopted [194]. The adsorption behaviour of cyanide during the electrodeposition has been investigated by in-situ Raman spectroscopy [226]. Baths for the codeposition of nanocrystalline Au with micrometric B_4C have been developed. Peculiar electrokinetic effects have been observed and modelled [244, 261].

The effects of organic additives on the crystal and crystallite structure have been investigated by XRD, SEM and in-situ SERS. These structural effects have been explained on the basis of competitive adsorption and cathodic reaction of the organics [194, 195, 226]. The nanocrystallinity of the electrodeposits and their preferred orientation can be controlled through the additive system. In-situ SERS measurements have highlighted the molecular aspects of grain growth inhibition and related stabilisation of adatom clusters and nanocrystalline structures [194]. A specific section of this paper (Section 5) will be devoted to in-situ spectroelectrochemical investigations relevant to the formation of nanocrystalline gold and alloy electrodeposits. Considerable stabilisation of nanograin dimensions under prolonged heat treatment can be obtained by dispersion of ceramic particles within the nanocrystalline matrix [262].

Hardness, Young modulus and plasticity of freestanding nanocrystalline metal and composite foils have been evaluated by instrumented indentation measurements [11]. The wear behaviour of nanocrystalline electrodeposited Au and Au/B_4C composites has been evaluated by the pin-on-disk method. Hardness values typical of nanometric systems can be preserved even after prolonged heat treatment in composite systems.

4.1.1. Au-Cu-Cd

Free-cyanide baths have been studied, with special emphasis on the control of the hydrodynamic conditions [63, 263, 264]. The formation of disordered fcc solid solutions as a function of galvanostatic electrodeposition conditions has been investigated by XRD [263]. Hardness, Young modulus and plasticity of nanocrystalline layers have been evaluated by instrumented indentation measurements [260, 263]. The tribological behaviour of 14, 18 and 23 carat alloy layers has been studied [260]. Microcutting and interfacial decohesion failure modes have been recognised as characteristic for the application of low and high loads, respectively.

4.1.2. Au-Cu

Baths based on $Au(CN)_2^-$, Cu(I)-CN^-, Cu(II)-EDTA and Cu(II)-DTPA have been developed for the electrodeposition of equiatomic alloys [13, 14, 245]. The addition of heavy metals and surfactants has been investigated with the purpose of minimising hydrogen uptake [261]. UPD behaviour of Cu has been observed, influencing alloy formation [97]. Systems for the codeposition of the nanometric alloy with micrometric B_4C have also been studied [13, 14].

The crystallographic structure of alloys deposited from free cyanide [13] and cyanocomplex [14] baths have been studied by XRD and DSC. Ordering, grain growth and development of antiphase boundaries as a function of heat treatment temperature and time have been followed. The effects of the dispersion of ceramic particles on structure evolution kinetics have been investigated. Hydrogen-related nanometric voids and their annealing behaviour have been investigated by thermal desorption spectroscopy and SAXS [250]. The effects of the nature of chelating agents on geminate density was studied by XRD peak analysis [241]. The presence of dispersed micrometric B_4C powders has been shown to favour room-temperature recrystallisation of initially nanocrystalline alloys [13, 14].

Instrumented indentation techniques and tensile testing have shown mechanical effects connected to the use of different Cu(II) chelating agents, which can be explained with different densities of hydrogen-related nanovoids present in the electroformed alloys [241].

4.1.3. Au-Sn

Alkaline baths have been developed containing Au(I) and Sn(IV) complexes. The various equilibrium intermetallics of the binary system could be obtained, the detection of these phases was performed by XRD and stripping voltammetry [98].

4.2. Co

Watt's type baths have been used. Galvanostatic deposition from a boric-acid containing solution [265] and potentiostatic deposition from a citrate containing electrolyte have been reported [70]. Pulse plating has also been applied to the citrate solution [234]. The concentration of citrate

added to the sulphate bath anticorrelates with nanometric grain dimensions [70]. DSC measurements [234] showed a broad, low energy exothermic feature in the range ca. 423-573 K followed by a peak at ca. 623 K. Combined DSC-SAED analyses showed that the grain-growth exothermic peak is complete before the hcp to fcc transformation occurs.

4.2.1. Co-Cu

A sulphate-citrate bath was proposed. Electrodeposition was carried out galvanostatically. Nanogranular two-phase Cu-Co alloys (6-20 w% Cu) consisting of a mixture of fcc Cu and hcp Co have been reported [266].

4.2.2. Co-Ni-P

A chloride bath containing boric acid and NaH_2PO_2 has been studied [227]. Hypophosphite was shown to have a significant effect on growth morphology. As the concentration is increased, smooth deposits successively change to: dendritic, nodular and again smooth. Correspondingly, the cross sections show laminated features superimposed on columnar growth features. The crystalline structure can be either fcc or hcp, according to the dominating Fe-group metal content. The preferred orientation varies in a complex way with the bath and alloy composition. The deposition conditions are reported to have limited effects on the grain size of the alloys (ca. 50 nm). The magnetic properties are mainly affected by the amount of codeposited P.

4.2.3. Co-Pd

Baths containing Co-sulphamate and Pd amino-nitrite have been studied [267]. The interaction among electroreduction processes of the alloying metals and the crystalline structure of the deposits has been investigated. Nanocrystalline deposits with strong grain correlation con be obtained in a wide compositional range [62, 252]. High-Co deposits develop a {111} preferred orientation.

4.2.4. Co-Pt

Baths containing Co-sulphamate, Pt amino-nitrite and glycine have been studied, sodium hypophosphite has sometimes been added [267-269]. The correlation between complex formation in the baths and the growth of crystals with a fixed stoichiometry has been recognised. Suitable chemical reducing agents can be used for the control of nanocrystallinity [62, 252]. Low-Pt alloys are hcp, high-Pt ones are fcc. A discontinuous variation of the lattice parameters with alloy composition has been recognised and correlated to the formation of mixed complexes in the electrodeposition bath [269]. Strong preferred orientations and the development of columnar structures can be obtained with appropriate values of the plating variables. The control of the nanometric dimensions of the alloy

crystallites correlates with the achievement of outstanding magnetic properties suitable for longitudinal magnetic recording [270].

4.3. Cu

Acidic sulphate baths have been used, plating has been carried out onto anodised Ti [86] and physical vapour deposition Cu induction layers [48]. Pyrophosphate solutions have also been investigated [195]. Pulse-plating and organic additives have been studied [85].

Electrodeposition of bimodal nanograined structures was obtained, with simultaneous presence of coarse (500 nm) and n-metric (100 nm) grains [48], owing to the occurrence of abnormal crystal growth. Nanocrystal dimensions can differ between the substrate and surface sides of electrodeposits by a factor of two, the former dimensions being smaller [59]. Significant tensile strength has been reported due to small grain size and high defect density. The nature and concentration of organics added to the electrodeposition bath affect the nanograin dimensions [85]. Room temperature recrystallisation has been observed [165, 271]. This behaviour has a significant bearing on the stability of the electrical quantities of electronic devices implementing electrodeposited Cu, which tends to exhibit time-dependent properties. Annealing at moderate temperature is therefore common practice to avoid uncontrolled ageing of these materials. The development of a <100> texture under low-temperature annealing has been reported [272]. The annealing of 100 nm grain deposits up to 423 K displayed a limited (ca. 20%) grain growth and no measurable variation of yield strength, concomitantly a notable improvement of ductility and ultimate tensile strength was observed. Hall-Petch behaviour of hardness was reported [59]. In one instance, the nanometric dimensions of the grains were controlled by imposing the value of the cell voltage [48].

4.3.1. Cu-Fe

A sulphate-citrate bath was proposed. Galvanostatic electrodeposition was used [42]. Nanogranular two-phase Cu-Fe alloys (0-60 w% Cu) consisting of a mixture of fcc Cu ({111} preferred orientation) and bcc Fe ({211} preferred orientation) have been reported [42]. The granularity of the electrodeposits has been confirmed by the linear behaviour of Mössbauer spectra as a function of composition. For the lowest amounts of Fe, the details of the evolution of the magnetic moment of the alloys were obtained by SQUID magnetometry. Increase of $CuSO_4$ concentration has been shown to correlate with a decrease of grain dimensions.

4.3.2. Cu-Ni

A sulphate-citrate bath was studied, electrodeposition was carried out by pulse plating [216, 242, 251]. Single phase fcc alloys (26-36 w% Cu) with grain dimensions in the range 2.5-28.5 nm and <111> texture have been obtained. Smooth, bright and nodular deposits can be obtained by adjusting the pulse plating parameters. Tensile stress is higher for galvanostatically deposited layers in

comparison with pulse plated ones, frequency and internal stresses are anticorrelated [216]. The residual macro-stresses of a range of Ni-Cu alloys was studied by spiral contractometry and the micro-stresses were measured by the peak-broadening of XRD peaks [251]. These residual stresses were shown to be invariably tensile in nature. The details of grain non-uniformity were studied by PAC, by doping equiatomic Ni-Cu alloys with $^{111}InCl_3$ added to the electrolyte [242]. Hyperfine interactions were detected, due to a disordered grain boundary structure could be observed. The presence of Ni precipitates below the detectability limit of XRD was inferred from PAC measurements. It was also shown that the homogeneity of the NiCu alloy could be improved by the use of low current densities, higher temperatures and addition of saccharin.

4.3.3. Cu-Sb

A sulphate-citrate bath has been developed for the galvanostatic electrodeposition of alloys in a wide compositional range [62]. Correlations have been studied among electrodeposition kinetics, morphology and formation of supersaturated solid solutions. Under particular plating conditions the spontaneous formation of multilayered structures with nanometric period has been observed.

4.4. Fe

An acidic Fe(II) bath containing citrate and boric acid has been described in [56]. Pulse plating with on and off times in the range of ms have been applied. Grain dimensions around 20 nm have been reported.

The thermal stability of the nanograin distribution was evaluated by real-time synchrotron XRD and peak shape analysis of the (110) and (220) reflections. Below 550 K the structure is thermally stable. At ca. 660 K a limited, asymptotic grain growth (to ca. 100 nm) is observed with some degree of broadening of the grain-size distribution. At ca. 780 K grain growth is initially fast and then slowly and asymptotically tends to ca. 400 nm. The grain-size distribution broadens considerably. In all the cases, the grain-size distribution is monomodal, denoting normal grain growth. The microstrains of as-plated nanocrystalline Fe are moderate (ca. 0.7%) and their relaxation upon heating can be separated into two parts: one with a small time constant - which has been interpreted in terms of irreversible, local single-atom jumps in the grain boundaries - and a second one not exhibiting an obvious time variation. Pronounced intergranular brittleness associates with segregation of interstitial impurities.

4.4.1. Fe-Ni

Watt's type baths have been employed [41, 62, 272]. Citrate and saccharine have been sometimes added to Watt's baths [238]. Additive-free all chloride baths have also been considered [60, 187]. Electrodeposition has always been carried out galvanostatically, generally at high current densities.

In the growth of highly stressed solid solution 13 w% Ni films, cracking has been reported for thicknesses in excess of ca. 1 μm [41]. Interestingly, cross sectional optical micrographs of the cracks reveal that they extend perpendicularly through only a fraction (ca. 10%) of the coating thickness. Cross-sectional TEM micrographs revealed a lamellar substructure with individual layers of thickness 100-400 nm, parallel to the substrate. Pure γ-phase as-plated 45 w% Fe deposits were obtained [238]. Formation of the α-phase was detected by annealing at 573 and 673 K for 20 h. Dominating <100> and <111> textures were observed. These textures are unexpected for a high-overvoltage electrodeposition system. Again unexpectedly, the <111> texture is stabilised by heat-treatments. The texture evolution during annealing has been studied for 78% Ni nanocrystalline permalloy [273]. The as-plated structure exhibits a strong <100> texture and a weak <111> one. Grain growth and the change of texture to <111> was observed for temperatures in excess of 613 K. Abnormal growth of the <111> oriented grains was noticed. As far as the grain dimensions are concerned, annealing at 573 K causes a gradual increase in grain size up to ca. 10 nm after 20 h [238]. During annealing at 673 K, grain growth to ca. 17 nm is observed in 0.5 h, further grain growth was slow and 20 nm were obtained after 20 h. The evolution of the Vickers microhardness closely follows the variation of the grain dimensions. The development of microstructure and texture of nanocrystalline Ni-Fe electrodeposits has been simulated by the Monte-Carlo technique for compositions around 20 w% Fe range [274]. 12-15 w% Ni deposits with grain dimensions 6-7 nm exhibit high internal stresses and microcracking [187]. Grain dimensions are anticorrelated with the current density. Stresses are higher for lower deposit thicknesses. A limited amount of stress relief is achieved by cracking, and by plating at higher current densities. Pure α-Fe solid solution, with dominant <111> and secondary <211> textures were observed. This is an out-of-equilibrium condition, since the equilibrium phase structure is two-phase with α and γ. The in-thickness compositional segregation which is typical for coarse-grained electrodeposited alloys is absent in this nanoelectrodeposited system. Mirror-like finish is achieved with minor growth features, hardly observable by TEM. Crack networks and in-thickness behaviour of the kind reported above [41] are recognised in this system, with a typical crack linear number-density of ca. 100 mm^{-1}. SEM micrographs of fracture surfaces reveal brittle fracture features with flat areas connecting the network of pre-existing microcracks, forming a terrace-like morphology. TEM replicas of etched cross sections reveal a multilayered structure with period ca. 100-400 nm; these sublayers contain globular features whose dimensions are ca. 20-50 nm, similar to the nanometric grain dimensions detected by Scherrer analysis of XRD peak broadening [60].

The Vickers hardness of 12-15 w% Ni layers [60, 187] lies in the range 650-700 HV and follows the Hall-Petch relationship. The nanocrystalline structure of these alloys leads to an enhancement of the magnetic properties and of the wear resistance for magnetic recording applications.

4.5. Ni

The Watt's bath has been widely employed for nanoelectrodeposition. Typical operating conditions are: room-temperature, galvanostatic deposition with high current densities. Additive-free

baths have been used either galvanostatically [94] or with pulse-plating [231, 242, 249, 275]. Use of saccharin and pulse plating have been reported [35, 220-222]. Saccharin and sodium lauryl sulphonate have been employed in [29, 237, 276]. Some degree of batch-dependence of contaminant level and nanocrystal dimensions has been pointed out in for replicated electrodeposition runs [237]. Sulphamate baths in a wide range of acidic pH values with commercial anti-pitting agents have been considered; galvanostatic electrodeposition was carried out at intermediate current densities in a rotating disk assembly [8]. Nanocrystalline Ni has been used as a matrix with dispersion of submicrometric alumina [277] and SiC [230, 239].

Crystallographic texture measurements were employed to assess the annealing properties of nanocrystalline electrodeposited Ni (starting grain size: unimodal 50 nm, bimodal 100 nm / 4 μm) and <100>+<111> texture [9, 94, 257]. This bimodal structure displays textured microcrystals and disoriented nanocrystals [9]. The presence of sulphur-containing organic additives has been related to the development of <200> texture, correlating to fibre structure assessed by TEM [237]. Annealing correlates with the growth of the <111> component in unimodal nanocrysalline samples [8, 9, 257]; rapid annealing gives rise to the <311> instead of the <111> texture [9]. The <211> texture develops in bimodal nano- and microcrystalline samples. Low thermal stability was demonstrated for bimodal structures and higher thermal stability for unimodal ones. Details of the texture evolution in micrometric bumps electroformed by through-mask plating are reported, typically texture variation kinetics is faster in electrodeposits with posts than in the flat ones. A detailed analysis of grain boundary misorientation and of atomic arrangement at grain boundaries shows that grain boundaries with misorientation angles between 30 and 45° have high mobility and control the texture transformation. Porosity at grain boundaries has been observed by TEM (1-2 nm) and positron annihilation (1 nm) for as-plated materials [237] and commonly tends to develop after heat treatment at 673 K [9]. Porosity of as-plated Ni has been related to the incorporation of hydrogen [237]. The <111> texture of nanoelectrodeposited Ni (32 nm) has been shown to favour the formation of highly protective NiO layers [8]. Besides texture, corrosion resistance of nanocrystalline electrodeposited Ni has been shown to depend on grain size [278], probably owing to the surface concentration of crystalline defects [279]. Moiré fringes have been observed by TEM [17] in the microstructure of nanoelectrodeposited Ni, suggesting that the nanograins are only slightly misoriented to each other; this has been recognised as a typical feature of nanocrystalline metals grown by electrodeposition. Nanoelectrodeposited Ni with initial grain size of 10-30 nm exhibits abnormal grain growth by a quasi-nucleation growth processes [17, 19, 240]. This phenomenon has been reported to occur at temperatures above 473 K [19] and at ca. 658 K [17]. A detailed kinetic analysis of abnormal growth behaviour by TEM has been reported in [231]. Annealing at 693 K for times in the range 1-30 s gives rise to a first kind of abnormal growth with a bimodal grain distribution peaking at 20 and 350 nm. Beyond this point and until 4 ks, the growth continues normally with a lower rate and mean grain size around 500 nm. Between 4 and 40 ks a second type of abnormal growth is active bringing about the formation of a bimodal structure with large planar grains (5-50 μm) and blocked grains of ca. 500 nm. By 432 ks the large abnormally growing grains have used up the matrix of submicron-sized grains and a uniform structure results with dimensions in the range 20-60 μm. It is interesting to note that several matrix grains are embedded rather than consumed by the abnormally growing grains. Conventional

electrodeposited Ni, which most probably contains some fraction of nanosize material, has been reported to exhibit grain growth at 373 K and recrystallisation at temperatures as low as 473 K [280]. It is not yet full assessed if abnormal nucleation is due to impurity segregation, even though some pioneering work by the three-dimensional atom probe method showed that no grain-boundary segregation can be observed in as deposited Ni, low levels can develop after annealing [240]. EDX mapping showed the presence of a second phase enriched in sulphur at growth interfaces during abnormal grain growth [231], this phase seems to wet the interface and to extend across more than one grain boundary segment. This phenomenon might be related to the formation of a sulphur-rich liquid Ni-S phase.

The static magnetic structure of nanocrystalline ferromagnets is generally highly nonuniform on a nanometer scale and this results in a strong elastic magnetic neutron scattering at small angles, which can give bulk structural information on the scale of a few nanometers [249]. Samples with average dimensions of ca. 50 nm, tested by small-angle neutron scattering display magnetic nonuniformities within the nanocrystalline grains. This internal nonuniformity can originate from twin-boundaries or from the nanocrystalline grain boundaries. By detecting the hyperfine interaction at the site of a suitable probe atom, such as PAC, information about the local structure of grain boundaries can be obtained, below the detectability limit of XRD [242]. Ni samples were suitably doped with ^{111}In. Phenomena related to a disordered bulk grain boundary structure could be observed. This behaviour was explained with the existence of four different ordered grain boundary structures.

DSC measurements showed a broad exothermic feature at ca. 373-498 K followed by a peak at ca. 543 K [21]. The starting feature has been explained with subgrain coalescence giving rise to the formation of nuclei which subsequently grow abnormally in the temperature range corresponding to the exothermic peak. Quantitatively different results have been reported in [17], where an exothermal irreversible structural change has been inferred from a heat-release DSC peak at ca. 606 K on the first heating scan, which disappears in the second one. The grain dimensions have been reported not to change from the initial value of 20 nm when the temperature is scanned in the DSC at 40 K min^{-1} below 533 K. Grain growth is observed when heating is continued to the range 593-613 K, corresponding to the DSC peak. The low misorientation boundaries of nanograins identified by TEM Moiré patterns act as nucleation sites for grain growth during annealing. These grains can easily rearrange their orientations and merge into larger grains giving rise to subgrain coalescence. Grain sizes in excess of 1 μm can be obtained by heating to 628 K during DSC measurements at the same heating rate. At higher temperatures normal grain growth is observed.

The temperature dependent linear coefficient of thermal expansion and the isobaric heat capacity have been measured [248]. The orientation dependence of the coefficient of thermal expansion during annealing was also investigated [257]. These properties are not measurably affected by grain dimensions. This confirms that the reported variations for different materials are reasonably due to porosity-related artefacts. The high density of intercrystalline defects present in the bulk and intersecting the free surface of nanoelectrodeposited materials brings about the fact that hydrogen transport rates and storage capacity in nanocrystalline Ni are considerably enhanced: six- to ten-fold increases in hydrogen diffusivity and 60-fold increase in hydrogen storage capacity have been reported [281, 282]. The self-diffusivity of triple lines in nanoelectrodeposited Ni has been reported to be three

times greater than that of grain boundaries in conventional Ni [281]. A higher electrocatalytic behaviour has been noticed with regard to the hydrogen evolution reaction for alkaline water electrolysis [282].

In composites with nanocrystalline Ni matrix and dispersion of nanometric SiC [239] SEM micrography revealed a typical microstructure consisting of irregularly shaped particles and agglomerates of SiC embedded in the nanocrystalline matrix. The nanometric grain dimensions of pure matrix deposits tend to be larger than those of composite samples produced under otherwise identical plating conditions (10-40 v 10-15 nm).

Regarding mechanical properties, high-strength coatings and freestanding structural components have been produced by electrodeposited Ni with grain sizes in the range 10-100 nm. Remarkable improvements in resistance-related quantities have been reported, anticorrelated with grain dimensions including: hardness, yield stress and ultimate tensile stress (increased up to a factor of five). As far as hardness is concerned, the consistency of experimental data with the Hall-Petch model has been insightfully discussed in [29, 35, 183]. A detailed analysis of the dependence of hardness on grain size obtained by heat treatment is reported in [9]. The onset of abnormal grain growth can be accompanied by hardening of the material, even though extensive annealing give rise to softening [240]. The cross-over in nanograin dimensions for inversion of the Hall-Petch behaviour has been measured [183, 220, 221, 283, 284] at ca. 10-20 nm. Modelling of the inverse Hall-Petch behaviour has been proposed [53]. This approach uses grains modelled as regular tetrakaidecahedra and, assuming a grain boundary thickness of 1 nm, shows that the grain boundary volume fraction increases rapidly from a few percent at a grain size of 100 nm to over 50% at a grain size of 2 nm. For grain sizes below 20 nm, the triple junction volume fraction reaches significant values and exhibits a greater grain size dependence than does the grain boundary volume fraction. Significant strain-hardening of this material has been reported in comparison with conventional Ni [29, 255]. Reducing the temperature to cryogenic values markedly increases the strain-hardening; this behaviour has been correlated with the grain-size dependence of the total activation energy for deformation of nanoelectrodeposited Ni. The ductility of this material has been shown to decrease with grain dimensions. The practical ductility of the material can nevertheless be significantly improved either by grain boundary sliding [228] or by the removal of plastic instabilities [285], even though in some cases (grain dimensions in the range 35-100 nm) [29] localised necking has been acknowledged as the main cause of low ductility. The fatigue behaviour of electrodeposits with grain sizes in the range 50-100 nm was measured in high cycle, fully reversed bending with stresses reaching the yield value [286]. Identical properties were found for nanoelectrodeposited and metallurgical Ni in corresponcence of the same hardness values (high hardness of metallurgical Ni was obtained by plastic deformation). Thus, neither accelerated fatigue associated with grain boundaries nor delayed failure due to some peculiar dislocation behaviour of the nanomaterial were recognised. Nanocrystalline (6-40 nm) electrodeposited Ni exhibits room-temperature creep under static and dynamic uniaxial loading [237, 255]. This behaviour has been explained with grain boundary sliding and intercrystalline diffusive material transport. The operation of dynamic processes is confirmed by the high strain- and loading-rate sensitivity: the width of the stress-strain loop is anticorrelated and the yield strength is positively correlated with the loading-rate. Rate sensitivity is especially marked for the smaller grain dimensions

(<20 nm) and it has been explained as due to a larger contribution of dynamic creep strain to the overall strain at a given stress level [255]. The strain-rate sensitivity has been reported to be one order of magnitude higher for nanocrystalline as compared to coarse-grained Ni. At higher strain rates the UTS increases for both nano- and coarse-grained Ni [237]. Compared to metallurgical polycrystalline Ni, nanoelectrodeposited Ni exhibits drastically reduced abrasive wear rates as determined by Taber [35], pin-on-disk [259] and nanoscratch [183] tests. Nanoelectrodeposits with grain dimensions of 13 nm exhibit small wear grooves and negligible plastic deformation, while samples with grains in the range 60-250 nm show limited side-ridge formation and some degree of plastic flow [35]. Even though different wear mechanisms were observed as a function of grain dimensions, the abrasive wear rate relates to hardness according to the Archard law [183, 287]. Lower friction coefficients have also been reported, measured by the pin-on-disk [259] method. No measurable variations of friction coefficient between n-crystalline (12-22 nm) and annealed metallurgical samples could be assessed by nanoscratching [183]. The fracture behaviour of 20 nm grained freestanding dogbone samples pulled at low and high strain rates show two types of morphology in the first case (rough and columnar) at different locations of the fracture surface and one (rough) in the latter [237]. This behaviour hints at the fact that nanocrystalline features of different dimensions might play a role in the deformation behaviour.

Composites with nanocristalline Ni matrix and dispersion of SiC showed substantial improvement in mechanical properties (hardness, yield and tensile stress) in comparison with composites with micrometric grain sizes of the matrix. It has been shown in [230, 239] that decreasing the grain size to the nanometric range has a greater hardening effect (more than a factor of 2) than adding a reinforcing phase to microcrystalline Ni: the hardness values for nanocrystalline Ni and SiC-containing composite are similar. The Orowan mechanism is unlikely to be operative in such nanocomposites since the reinforcing particles are typically one order of magnitude larger than the average matrix grain size. Some irregularities reported in the variation of Vickers hardness with SiC content, can be explained with differences of crystallographic texture which, in turn, correlate with the dispersoid volume fraction [239]. Adding SiC to nanocrystalline Ni does not have the same significant effect on increasing the yield strength as that of adding SiC to microcrystalline Ni. This difference can be expected since the onset of composite yielding in metal matrix ceramic particulate systems is controlled by the onset of matrix yielding which, for nanocrystalline materials, is not under the control of a dislocation mechanism since the grain size is too small. Nanocrystalline Ni/SiC samples with very low volume fractions of reinforcement exhibit relatively high tensile strength, this effects tends to be lost as the volume fraction increases above ca. 2 vol%. This effect can be related to particle agglomeration, giving rise to the formation of localised soft regions in the hard nanocrystalline Ni matrix. For these composites with SiC ca. 2 vol% an increase in tensile ductility was observed in comparison with pure nanoelectrodeposited Ni. At higher SiC contents the strength and ductility of the nanocomposite were found to decrease [230, 239]. This behaviour can be related to the removal of plastic instabilities, as pointed out in [285]. Fibrous cup-and-cone fracture surfaces have been recognised for low SiC contents in nanocrystalline Ni/SiC and cleavage-type facets for high particulate contents [239].

4.5.1. Ni-P

Watt's type baths have been employed with the addition of phosphorous acid [15, 40]. Nanocrystalline Ni-P has been used as a matrix with dispersion of submicrometric alumina [277] and SiC [15, 239].

Increasing the P content (1-22 at%) in Ni electrodeposits leads to grain refinement down to the amorphous state, passing though the nanometric range [40]; at all compositions a single-phase structure is obtained. The localisation of P atoms within nanometric grains has been measured by a special TOF-MS technique [222]. A nanoscale grained structure could be identified by tracing P isoconcentration surfaces at 6 at% P within nanometric grains of 4.3 at% P samples. No grain-boundary segregation of P could be observed. Some degree of grain-boundary segregation of P has been noticed after heat-treatment (523 K, 1 h) of the electrodeposits, together with Ni_3P precipitation. It is worth mentioning that grain-boundary segregation of P has been measured in as-plated electroless samples of approximately the same P content [288]. The tendency to grain-boundary segregation in these systems helps in thermally stabilising the nanograined structure, presumably by grain boundary pinning caused by solute drag (phosphorus atoms) and Zener drag (Ni_3P precipitates) [20]. Similarly, Ni-P (1.2 w% P) nanoelectrodeposits with grain size of 10 nm exhibit thermal stability up to 623 K, above which normal grain growth was observed [22]. The relationships among electrochemical kinetics and growth structure have been highlighted. The presence of dispersed micrometric B_4C powders has been shown to favour room-temperature recrystallisation of initially nanocrystalline alloys [15].

Creep of Ni-P, 20 at% P alloys with grain dimensions of 28 nm in the temperature range 543-593 K has been recognised. The creep mechanism has been identified as grain-boundary diffusion [256]. Inverse Hall-Petch behaviour, implying softening for grain dimensions smaller than 8 nm, has been reported for as-plated n-crystalline Ni-P [283]. Hardness, Young modulus and plasticity of Ni-P/B_4C composites have been evaluated by instrumented indentation measurements as a function of ceramic content [15]. The abrasive wear of nanocrystalline samples with P below 6 % was studied by the Taber method [258]. The samples showing the highest wear resistance in the as-plated state contained 1.8% P. Annealing at 646 K for 1 hour gives rise to an optimal precipitation of fine Ni_3P enhancing hardness and wear resistance.

The effects of structural and compositional disorder (induced by grain size refinement and alloying, respectively) on saturation magnetisation have been studied in [40]. A rapid decrease of saturation magnetisation with P content was observed. This magnetic property was not appreciably affected by grain dimensions.

4.5.2. Ni-W

Sulphate baths containing ammonium, citrate and bromide have been used, with additions of Na_2WO_4, galvanostatic deposition was carried out at high current densities [225, 228, 232, 289]. Appropriate values of citrate and Ni(II) concentrations were shown to lead to a minimisation of nanocrystal size and increase of cathodic efficiency in galvanostatic electrodeposition conditions

[289]. Compositionally graded nanocrystalline Ni-W alloys were obtained by changing the electrodeposition current density (50-120 mA cm^{-2}) and bath temperature (298-333 K) [232].

Nanocrystalline and X-ray amorphous Ni-W (5-30 at% W) have been obtained [225, 228]. The grain dimensions are negatively correlated with W content. X-ray amorphous samples might actually display atomic clustering giving rise to granularity with typical dimensions in the range of nanometers, as identified by SAXS [225, 235]. Inhomogeneities attributed to nanometer-sized voids, have been detected in the analysis of Guinier plots of SAXS results [235]. Controlled annealing of X-ray amorphous materials can be used to obtain nanometric grains of desired dimensions [225]. The nanocrystalline structure with grain dimensions of 10 nm is randomly oriented and is stable up to 873 K. The <111> texture develops with increasing W content, possibly owing to lower strain in this orientation [232]. The RDFs derived from EXAFS spectra of as-plated Ni-W alloys are very similar to those of crystalline Ni and Ni_4W [235]. No medium-range order around the W atom could be detected, indicating that there is a considerable deviation in the atomic distances around the W atom in electrodeposited Ni-W nanocrystalline alloys. The crystallisation of Ni-W nanocrystalline electrodeposits was shown by DTA to take place in two steps: at 982 K fcc Ni-W solid solution precipitates and at ca. 1100 K Ni_4W forms, correspondingly strong <111> fibre texture develops. Within the <111> texture, HRTEM analyses reveal that nanometric grains (ca. 6 nm) precipitated from X-ray amorphous alloys have a random orientation and intercrystalline regions 1-2 nm in width.

Nanoelectrodeposits with high hardness, good ductility and high tensile strength were obtained [228]. Grain refinement correlates with W content (in the range 18-23 at%) and current density. The hardness correlates with grain-dimensions in accord with the Hall-Petch relationship, with inversion at ca. 9-10 nm [225, 228]. Nanocrystalline deposits with compositions in the range W 10-20 % exhibit comparable hardness values [289]. The fracture strain is strongly negatively correlated with grain dimension. Incorporated hydrogen has been reported to bring about a strong reduction of tensile strength and ductility. Annealing at 698 K for 24 h caused a limited grain growth (from ca. 4 to ca 9 nm), correspondingly the Vickers hardness increased from ca. 650 to ca. 900 HV. The X-ray amorphous samples with 25 at% W have a hardness of 770 HV. Hardness further increases to 1450 HV upon nanocrystallisation heat treatment and subsequently decays owing to grain growth [225]. Heat treatment however brings about the embrittlement of these nanoelectrodeposits [228]. On annealing X-ray amorphous 25 at% W alloys at 623 K for 24 h, no evidence of crystallisation was obtained by DTA or XRD, nevertheless SAXS showed a larger spread of cluster dimensions, denoting enhanced cluster-formation activity.

4.6. Zn

Nanocrystalline Zn layers have been eledeposited by pulse plating from a chloride bath containing ammonium chloride, boric acid, polyacrylamide and thiourea [236]. A rotating-disk electrode has been used for the control of mass-transport conditions. Nancrystalline Zn (grain dimensions in the range 20-80 nm) could be obtained either by using high peak currents (2 A cm^{-2}) or by employing organic additives. Increasing peak current densities correlate to changes of preferred

orientation: (11.2), (11.0), (10.1). A systematic broadening of the XRD peaks with peak current density has been reported. The hardness of nanocrystalline Zn conforms with the Hall-Petch relationship in the investigated range of grain dimensions.

4.6.1. Zn-Mn

Sulphate-citrate electrolytes have been studied for the achievement of high-Mn contents [290, 291]. Additions of selenium compounds [292] and thiocarbamide [188] have been investigated.

A range of nanocrystalline equilibrium and non-equilibrium phases has been obtained, as a function of the galvanostatic electrodeposition conditions [188, 233, 290-294]. The thermal stability of nanosized grains and the evolution of internal stresses have been studied by XRD peak analysis [10]. The correlation among crystallite morphology, bath chemistry - in particular growth inhibitors - and plating conditions has been investigated [188, 290, 292, 294]. Nanometric pure ε-phase electrodeposits were prepared. The organic additive stabilises the nanocrystalline structure with high Mn contents. The morphology is characterised by small crystallites or cauliflower growth features, as a function of the plating conditions. Layers with good mechanical properties and high corrosion resistance are obtained [188].

4.6.2. Zn-Ni

Acid chloride baths were studied [61, 229, 295, 296]. Proprietary grain refiners and pulse plating were employed [295, 296].

By manipulating the pulse plating parameters the grain size can be changed in the range 20 nm-15 μm, in correspondence the alloy composition varies in the ranges 9-18 w% Ni [295, 296] and 55-63 w% Ni [229]. Higher Ni contents correlate with smaller grain sizes (reported down to 5 nm). Intermediate composition deposits, close to the composition of the γ intermetallic, display the largest grain dimensions. The deposits are in any case pure γ-phase with different preferred orientations, induced by the plating conditions. The thermal stability of the nanometric grain structure was studied by in-situ annealing in the TEM by exposition to the e-beam: grain growth form 5 to 80 nm was observed in 15 min [229]. Optimal corrosion behaviour of the smallest-grain system has also been shown [296].

Hardness follows the inverse Hall-Petch behaviour over a large crystal size range (20 nm - 5 μm), a combination of grain size and solid solution hardening mechanisms could account for this complex behaviour [295, 296]. Pure γ-phase deposits can be obtained with hardness of ca. 500 HV; hardness values in this range are obtained by a combination of solid solution hardening and grain size effects, which in principle might include both hardening and softening effects [229].

5. IN-SITU SPECTROELECTROCHEMICAL STUDIES OF NANOCRYSTALLINE METAL ELECTRODEPOSITION

Spectroelectrochemical SERS and FT-IR studies of metal electrodeposition are aimed at understanding the processes taking place at the electrochemical growth interface. Cathode inhibition and grain-growth control phenomena can thus be understood and controlled at a more fundamental level. In particular the development and stability of SERS-active growth features is closely related to the formation of nanocrystalline coinage metal and alloy electrodeposits.

Seminal studies have been carried out on Ag [297] and Au electrodeposition from $KAu(CN)_2$ [97, 99, 194, 253, 254] and $KAu(CN)_4$ [298] baths. Benzyldimethylphenylammonium chloride (BDMPAC) [253, 299] and Tl^+ [97, 99] have been considered as nanocrystal-size controlling additives.

5.1. Sers of CN^-

In this study, we take advantage both of the SERS activity of gold and of the surface roughness and nanometric morphology induced by the electrodeposition in progress. This implies the possibility of carrying out SERS measurements without need of roughening pre-treatments of the electrode and of gaining information on the electrochemical conditions for the onset of metal cluster formation and stable growth. The details of SERS activation and surface species formation can be followed by the analysis of the fine structure, intensity and Stark shift of the adsorbate bands of gold cyano- complexes and CN^-. The peculiarity of this study lies in the fact that the CN^- is not adsorbed on the surface from the bulk of the solution, but it is produced by the decomplexing reaction connected to the cathodic polarisation of the electrode. Four kinds of CN stretching bands have been identified, as a function of

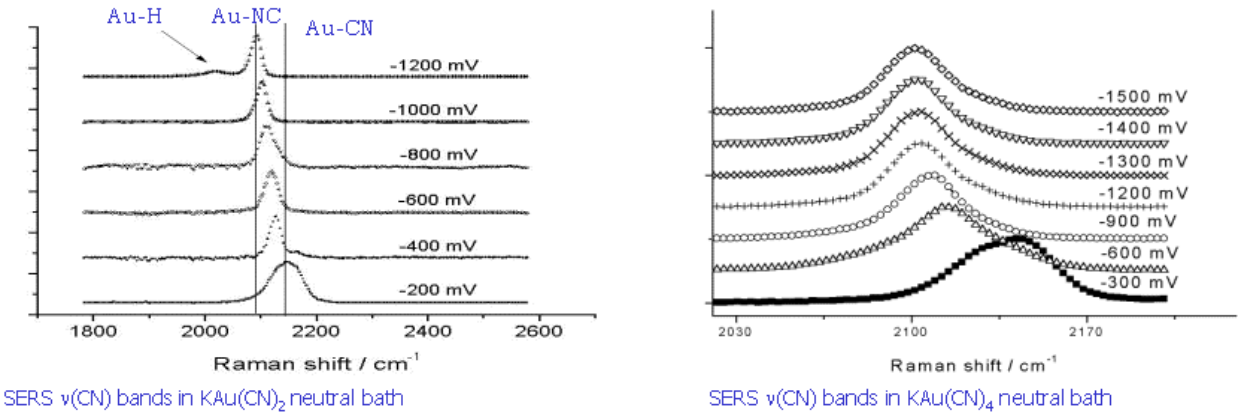

Figure 1. In-situ Raman spectra measured during potentiostatic electrodeposition (potential v Ag/AgCl).

electrodic potential. In the potential range where Au reduction takes place adsorbed CN^- can be bonded to the electrode surface either through its C-end or though its N-end [300], mainly owing to electrostatic reasons; at high cathodic potentials the Au-NC^- (2077-2156 cm^{-1} for $KAu(CN)_2$, 2102-2122 for $KAu(CN)_4$) species predominates. In the same region the presence of the Au-H stretching

peak (2014 cm^{-1}) can be noticed. An interval of potentials exists close to the equilibrium of the $Au(CN)_2^-$/Au couple (from –400 to 200 mV) in which Au-CN^- and Au-NC^- cohexist. At slightly anodic potentials the presence of both Au-NC^- and Au-CN^- (2133-2205 for $KAu(CN)_2$, 2142-2185 for $KAu(CN)_4$) can be detected and formation of $Au(CN)_2^-$ (2165-2171 cm^{-1}) can be noticed, owing to sluggish relaxation processes deriving from previous cathodic polarisation in the electrodeposition range of potentials. At more markedly anodic potentials, adsorbed cyanate (2217-2229 cm^{-1}) can be observed. The relevant SERS spectra for $KAu(CN)_2$ and $KAu(CN)_4$ baths are reported in Fig. 1.

5.2. Sers of bdmpac on Au

The electrochemical behaviour of several organic additives has been tested in our group as replacements of toxic heavy metal ions [245, 301, 302]. Among them BDMPAC [302] showed a remarkable depolarising and hydrogen-scavenging action (Fig. 2). Furthermore the preferential adsorption of this quaternary ammonium anion on open crystal faces induces peculiar crystal orientations and growth morphologies [194]. In this case the coadsorption of BDMPAC and of the CN^- resulting from the electrodeposition reaction proved to be the key-factor in the formation of nanocrystalline structures [253].

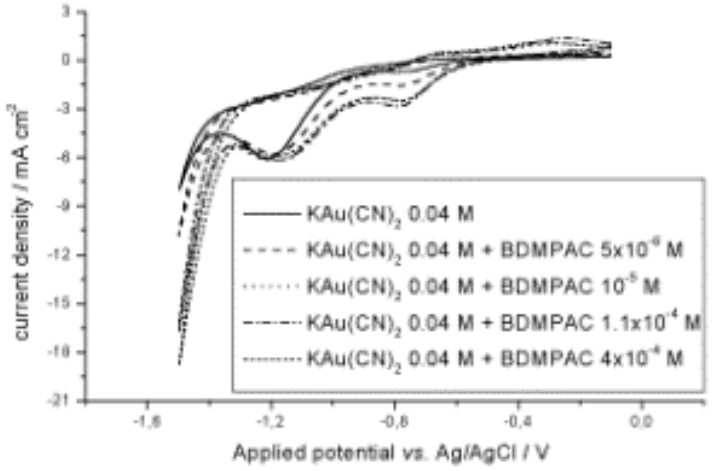

Figure 2. Cyclic voltammograms at a polycrystalline Au electrode with increasing concentrations of BDMPAC.

The vibrational bands of the quaternary ammonium salt appear in the potential-dependent spectra around the potential value at which the self-inhibiting reduction of Au(I) starts [97] (-900 mV (Ag/AgCl)). The aromatic bands are clearly visible. The inspection of the spectra reveals a neat change in the band pattern at a potential around –1300 mV (Fig. 3), which marks the beginning of the free growth of Au crystals and concomitantly, of the hydrogen evolution reaction. At potentials less cathodic than –1300 mV, a flat orientation of the benzyl ring – directly interacting with the metal

surface through the π-electron system – can be inferred from the downshifted ring breathing (989 cm^{-1}) and ring stretching (1588 cm^{-1}) bands, from the benzyl combination band (1212 cm^{-1}) and from the out-of-plane vibrational mode at 546 cm^{-1}. The weak band at 1485 cm^{-1} is typical for an in-plane deformation of a phenyl ring carrying an electrowithdrawing substituent and it has been attributed to the phenyl ring standing up on the surface. The modification of the band pattern around –1300 mV can be accounted for admitting that BDMPAC reacts on the electrode surface. In fact the set of bands present at less cathodic potentials is still present at cathodic polarisations beyond –1300 mV, together with the new ones; the relative intensities of the two sets of bands is about 0.5 for cognate vibrational modes. The disappearance of the peak at 1485 cm^{-1} is diagnostic of the fact that an elecronwithdrawing group on a benzene ring is transformed in an electrondonating one: this is the kind of transformation accomplished by a debenzylation reaction of a benzyl-phenyl quaternary ammonium salt. The bands appearing at potentials more cathodic than –1300 mV are indicative of a phenyl ring standing in upright position on the surface, because of the unshifted ring breathing and ring stretching modes with respect to the normal Raman values (1003, 1604 cm^{-1} respectively), the in-plane deformation modes at 623 cm^{-1} and 1155 cm^{-1}, the aliphatic and aromatic CH stretching bands (2800-3300 cm^{-1}). The band at 846 cm^{-1} matches well with the data found in literature for one of the typical bands of dimethylaniline. The analysis of the potential dependence of the CN^- stretching band, going towards cathodic potentials, shows that the inversion Au-CN^-/Au-NC^- occurs around –1300 mV, making the C-end of CN^- available for nucleophilic attack on another surface species.

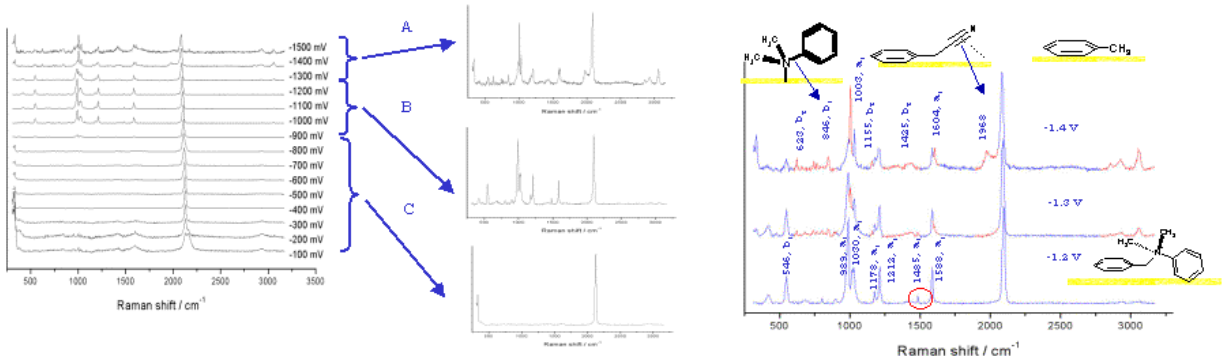

Figure 3. In-situ Raman spectra of BDMPAC and CN^- during potentiostatic electrodeposition from a $KAu(CN)_2$ bath (potential v Ag/AgCl).

We therefore concluded that electrocrystallisation is accompanied and affected by two surface reactions taking place at the threshold potential of –1300 mV: (i) a hydrogenation reaction, consuming surface hydrogen and producing dimethylaniline and toluene; (ii) a nucleophilic substitution carried out by the surface cyanide on the benzyl group and giving rise to dimethylaniline and phenylacetonitrile; this reaction consumes cyanide adsorbed on the electrode which is the cause of cathodic passivation. Dimethylaniline stands in upright orientation on the surface and interacts with it through the N lone pair, thus accounting for the observed spectral features; phenylacetonitrile has its

aromatic ring flat on the surface and the CN-group tilted at a certain angle, as shown by the band at 1968 cm^{-1}.

On the basis of these results, BDMPAC has been shown to provide surface scavenging activity towards hydrogen and cyanide, thus accounting for both the depolarising action and the lower incorporation of hydrogen in the deposit.

The adsorption and surface reaction scenario of BDMPAC on a polycrystalline gold electrode as revealed by SERS and differential capacitance experiments is very different in the absence of the electrocrystallisation reaction. BDMPAC adsorbs on the gold electrode in the potential range –1450/200 mV. A reorientation of the molecule can be inferred from the SERS spectra, in accordance with the differential capacitance curve features, which presents two adsorption minima separated by a desorption peak at the potential where the reorientation is observed spectroscopically (ca. –120 mV (Ag/AgCl)). From the spectral details reported in section *SERS-2* we could assign the interaction of the molecule with the gold surface through the π-electron system of the benzyl ring oriented flat on the surface in the potential range between –1450 and –200 mV. At more anodic potentials some straightforward spectral changes demonstrate a face-on/edge-on reorientation: (i) the ring breathing band at 1002 cm^{-1} - unshifted with respect to its normal Raman value - is seen to gradually replace the one at 992 cm^{-1}; (ii) the benzyl combination band at 1212 cm^{-1} progressively vanishes, while the band at 1177 cm^{-1} (an in-plane mode) can still be observed; (iii) the band at 540 cm^{-1} (out-of plane ring deformation) disappears. In particular, keeping in mind the shape of the capacitance curve, we envisaged the desorption of the benzyl ring in a face-on adsorption geometry and the subsequent adsorption of the phenyl ring in an edge-on orientation for more anodic potentials. No electrodic reactivity - and in particular no hydrogenation of the molecule - has been observed in the absence of the electrodeposition reaction.

5.3. Sers of Au-H

Several independent experiments prove that a peak at 2014 cm^{-1} appears during the electrodeposition of gold from $KAu(CN)_2$ when the potential is set in the hydrogen evolution region and that its intensity increases with increasing cathodic potential (Fig. 4) [253, 254]. Despite the low surface hydrogen concentration, the SERS mechanism, which acts on the active sites most probably responsible for the stabilisation of hydrogen adatoms, allows this peak to appear intense. A dramatic (95%) reduction in intensity of this peak can be observed when BDMPAC is added to the deposition bath. This fact straightforwardly correlates with thermal desorption spectra [301] which reveal that one of the two hydrogen traps found in the deposit from the BDMPAC-free bath, is eliminated by the use of this additive.

5.4. Stark tuning of CN^-

We investigated the potential dependence of the surface CN^- stretching band [97, 194, 302] for the different cyanide species identified during the electrodeposition process in three different baths:

$KAu(CN)_2$, $KAu(CN)_4$ and $KAu(CN)_2$ with BDMPAC. Stark slope values and their 99% confidence intervals are reported in Fig. 5. One can observe that the Stark slope found for each CN^- species in the three studied systems is different: this suggests the possibility of employing the Stark tuning as a diagnostic parameter for a detailed recognition of the morphological and chemical nature of the environment of the species involved in electrodic processes in different potential ranges. Changes in the potential dependence of peak position can be essentially interpreted in terms of differences of SERS-active sites and coadsorption effects [298].

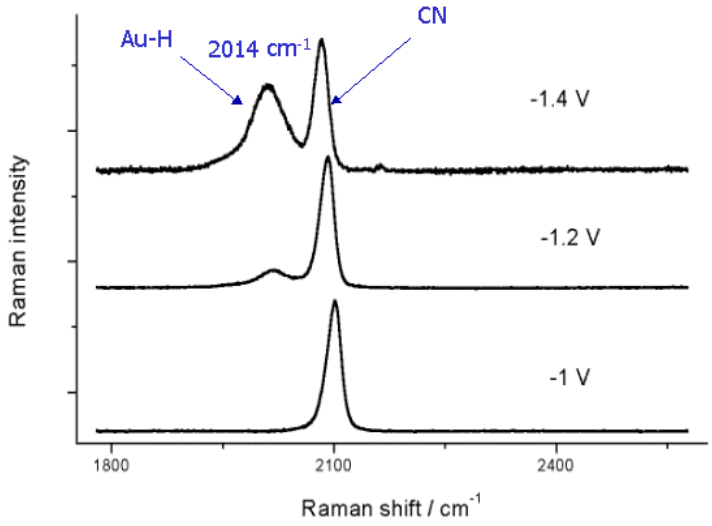

Figure 4. In-situ Raman spectra of the ν(Au-H) and ν(CN) bands in the hydrogen evolution potential range measured in a $KAu(CN)_2$ bath (potential v Ag/AgCl).

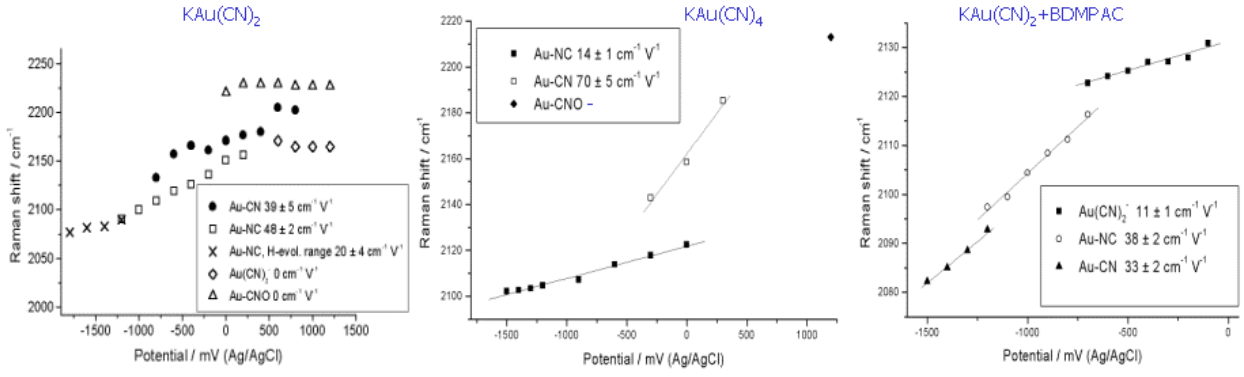

Figure 5. Stark tuning of the ν(CN) band measured by in-situ Raman spectroscopy for $KAu(CN)_2$, (without and with BDMPAC) and $KAu(CN)_4$ solutions.

5.5. FT-IR of the Au/Tl system

Addition of Tl^+ to $KAu(CN)_2$ baths has been shown to bring about an enhancement of the growth rate [97]. Vibrational in-situ spectroscopy [99] proved helpful for the understanding of the mechanism accomplishing these effects. In particular, this is a case in which the complementarity of FT-IR and SERS reveals its power, since Tl UPD hampers the SERS effect and the field confinement related to the thin layer set-up for in-situ IR experiments can be used to record spectra simultaneously from unscreened and screened areas of the electrode thus simulating passivated and free growth regimes. In-situ FT-IR spectra (Fig. 6) at cathodic potentials (-500 mV) show that a Tl UPD layer forms on the gold surface, competing with CN^- adsorption. Since this species is the one actually responsible for the cathodic passivation (decrease of the band at 2123 cm^{-1}), simultaneously an increasing reaction rate is witnessed by the increase of the band at 2093 cm^{-1} (Au-NC^-, which is formed during the electrodeposition); and a band related to free cyanide (2080 cm^{-1}) delivered by electroreduction is present and its intensity are connected to the presence of Tl. The mechanism suggested to account for these observations implies that the CN^- species adsorbed though its N-end and formed in the electroactive area of the electrode surface tends to migrate to the zero-field area of the electrode where it tends to convert into Au-CN^-. The UPD of Tl competes with the formation of the Au-CN^- bond, after the Au-NC^- one is broken, thus destabilising the Au-CN^- species and providing a renewed metal surface onto which electroreduction can proceed. No traces of thallium are found in the deposit, by a host of surface analysis techniques. This suggests that the Tl adlayer is displaced by Au(I) giving rise to a cyclic electroreduction/passivation/reactivation/displacement mechanism ensues. A similar action has been proved for other metals giving rise to UPD behaviour on gold, by different techniques [97].

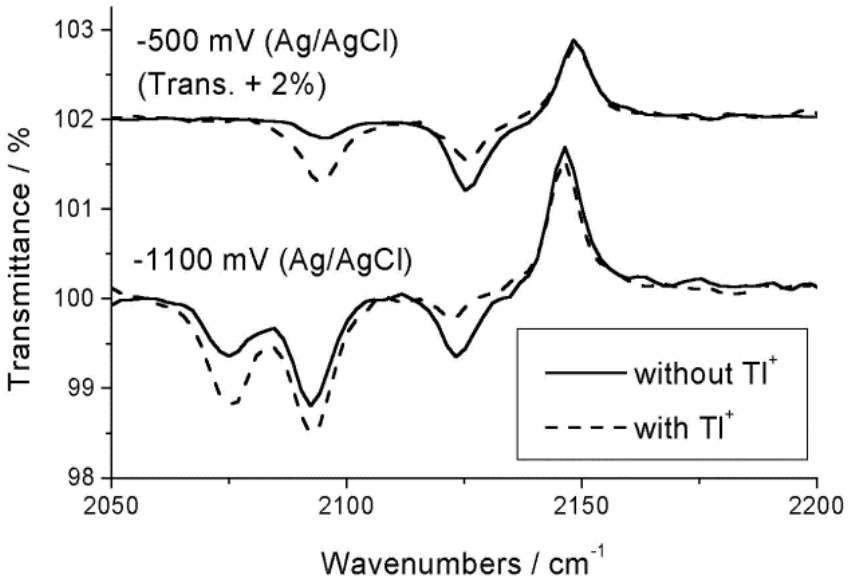

Figure 6. In-situ FT-IR spectra measured in a $KAu(CN)_2$ without and with Tl^+.

5.6. FT-IR studies of the anodic behaviour of nanocrystalline gold

Nanocrystalline gold grown by electrodeposition also displays a different anodic behaviour in CN^- solutions, giving rise to different oxidation products with respect to conventional macrocrystalline gold. The nature of the CN^- species present at the gold electrode/electrolyte interface in a KCN solution in the range -200 / -800 mV (Ag/AgCl) has been investigated by in-situ FT-IR in the case of a micro-crystalline annealed gold electrode and in the case of a nano-crystalline electrode obtained by electrodeposition. The potential-dependent spectra shown in Fig. 7 are ratioed over the spectrum recorded at –1.3 V (Ag/AgCl), potential at which cyanide is adsorbed. Several ν(CN) bands can be noticed for both micro- and nano-crystalline Au, corresponding to the following species: free CN^- (2080 cm^{-1}), CN^- adsorbed on Au (2085-2125 cm^{-1}) and $Au(CN)_2^-$ (2146 cm^{-1}) deriving from gold oxidation. A new band at 2161 cm^{-1} can be observed only in the case of nano-crystalline gold. This band can be tentatively attributed to a AuCN film formed on the electrode in analogy with the values reported for CuCN (2170 cm^{-1}) and AgCN films (2167 cm^{-1}) [303].

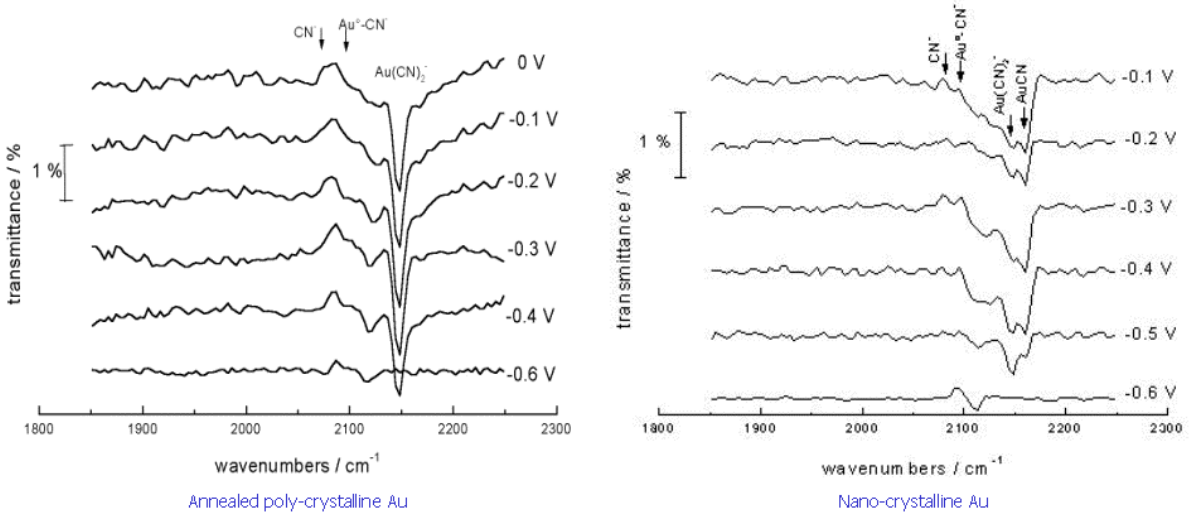

Figure 7. In-situ FT-IR spectra of CN^- species adsorbed on polycrystalline (metallurgical) and nanocrystalline (electrodeposited) Au.

6. CONCLUSIONS AND OUTLOOK

At the time of this writing, the electrodeposition of nanocrystalline metals and alloys is probably the only mature nanotechnology, producing a broad range of materials which find extensive practical application in many fields of the industry, spanning both high- and low-technology areas. Still, there is much scope for knowledge-driven innovation in this field. The industry actually awaits contributions from both fundamental science and technology, in order to bring new or improved processes and materials to the market. The principal scientific concern relates to gaining control over

the structural evolution of nanocrystalline electrodeposits - in order to improve the stability of their outstanding functional properties - and to defining accurate and predictive correlations among processing conditions and structural features. This field is in fact daunted with ubiquitous pseudo-correlations in the relevant literature, which often obscure otherwise sound experimental facts and prove misleading for further research. Owing to the multidisciplinary nature of the field, considerable scatter in research approaches and publication means sometimes cause limited contact among cognate research groups, rediscoveries and - often apparent - inconsistencies of results and interpretations. Research and development in the field suffer under the lack of a firm rationalisation of the technology. This problem is probably typical for applied electrochemistry of materials and some delays in achieving high-technology standards in the corresponding industries may stem hence.

A molecular-level approach to topics of immediate relevance for the applications is not wishful thinking in this field and the use of cutting-edge research tools can easily and quickly prove rewarding. From the technological point of view, process control and multiscale engineering are the key issues. A typical application-scale process implies keeping control over nanometric grains, micrometric crystallites and centimeter-scale current density and fluid-flow distributions. Full processing optimisation and reproducibility can be achieved only if non-empirical control is gained over nanoscaled features. Explicit consideration of the nanoscale is typically omitted when the focus is on application-oriented quantities, such as, e.g. hardness. The nanoscale is thus effectively a latent variable which is often out of control, in practice. As far as the perspective developments of this field are concerned, the relative simplicity of electrodeposition processes and the flexibility of the processing equipment warrant a limited time-to-market and offer an opportunity of inexpensively building the results of basic science into the final products. These dynamic features of the innovation process in the electrodeposition of nanostructured metals probably means the competitive margin of this technology with respect to vacuum, powder-compaction and melt-spinning approaches.

References

1. R.W. Siegel, *NanoStructured Materials* 3 (1993) 1
2. D. Fiorani and G. Sberveglieri ed.s, Fundamental Properties of Nanostructured Materials, World Scientific, Singapore (1994)
3. H. Gleiter, *Mater. Sci. Forum* 189-190 (1995) 67
4. D.G. Morris, Mechanical Behaviour of Nanostructured Materials, Trans Tech Publications, Zürich-CH (1998)
5. Z.L. Wang, ed., Characterization of Nanophase Materials, Wiley-VCH, Weinheim (D) (2000)
6. H. Gleiter, *Prog. Mater. Sci*. 33(1989) 223
7. J.A. Eastman, M.R. Fitzsimmons and L.J. Thompson, *Philos. Mag*. B66 (1992) 667
8. F. Czerwinski, G. Palumbo and J.A. Szpunar, *Scripta Mater*. 39 (1998) 1359
9. F. Czerwinski, A. Zielinska-Lipiec and J.A. Szpunar, *Acta Mater*. 47(1999) 2553
10. B. Bozzini, P.L. Cavallotti and F. Pavan, *Journal de Chimie Physique* 94(1997) 1009
11. B. Bozzini, G. Giovannelli, M. Boniardi and P.L. Cavallotti, *Composites Science and Technology* 59(1999) 1579
12. J.L. Delplancke, V. Di Bella, J. Reisse and R. Winand, *Mater. Res. Soc. Symp. Proc*. 372(1995)75
13. B. Bozzini, G. Giovannelli and P.L. Cavallotti, *J. Appl. Electrochem*. 29(1999) 685

14. B. Bozzini, G.Giovannelli and P.L. Cavallotti, *J. Appl. Electrochem*. 30(2000)591
15. B. Bozzini, P.L. Cavallotti and G. Parisi, *British Corrosion Journal* 36(2001)49
16. L.C. Chen and F. Spaepen, *J. Appl. Phys*. 69(1991)679
17. N. Wang, Z. Wang, K.T. Aust and U. Erb, *Acta Mater*. 45(1997)1655
18. K. Lu, W.D. Wei and J.T. Wang, *J. Appl. Phys*. 69(1991)7345
19. R.S. Averback, H.J. Hoefler, H. Hahn and J.C. Logas, *NanoStructured Materials* 1(1992)173
20. K. Boylan, D. Ostrander, U. Erb, G. Palumbo and K.T. Aust, *Scripta Metall.* 25(1991)2711
21. U. Klement, U. Erb, A.M. El-Sherik and K.T. Aust, *Mater. Sci. and Eng*. A203(1995) 177
22. S.C. Mehta, D.A. Smith and U. Erb, *Mater. Sci. and Eng*. A203(1995)227
23. H. Kung. Proc, TMS Fall Meeting, Cincinnati (1999)
24. H. Van Swygenhoven and A. Caro, *Phys. Rev*. B58(1998)11246
25. H. Van Swygenhoven, D. Farkas and A. Caro, *Phys. Rev*. B62(2000) 831
26. V.Y. Gertsman, M. Hoffman, H. Gleiter and R. Birringer, *Acta Metall. et Mater*. 42(1994) 3539
27. R.Z. Valiev, O.V. Mishin and R.M. Gayanov, *Mater. Sci. Forum* 170-172(1994) 83
28. A.H. Chokshi, A. Rosen, J. Karch and H. Gleiter, *Scripta Metall*. 23(1989)1679
29. F. Ebrahimi, G.R. Bourne, M.S. Kelly and T.E. Matthews, *NanoStructured Materials* 11 (1999)343
30. R.C. Gifkins, *J. Am. Ceram. Soc*. 51(1968) 69
31. H. Lüthy, R.A. White and O.D. Sherby, *Mater. Sci. and Eng*. 39(1979) 211
32. J. Horvath, R. Birringer and H. Gleiter, *Solid State Commun*. 62(1987) 319
33. K. Jia and T.E. Fischer, *Wear* 203-204(1997) 310
34. Z.N. Farhat, Y. Ding, D.O. Northwood and A.T. Alpas, *Mater. Sci. and Eng*. A206(1996)302
35. D.H. Jeong, F. Gonzales, G. Palumbo, K.T. Aust and U. Erb, *Scripta Mater*. 44(2001)493
36. A.W. Ruff, in: Mechanical Properties and Deformation Behaviour of Materials Having Ultra-Fine Microstructures, M. Nastasi, D.M. Parkin, H. Gleiter ed.s, NATO AIS Series (1993), Vol. 233, p. 199.
37. F. Czerwinski, *J. Electrochem. Soc*. 143(1996) 3327
38. U. Admon, M.P. Dariel, E. Grunbaum and J.C. Lodder, *J. Appl. Phys*. 62(1987)1943
39. B. Szpunar, U. Erb, G. Palumbo, K.T. Aust and L.J. Lewis, *Phys. Rev*. B53(1996)5547
40. B. Szpunar, M. Aus, C. Cheung, U. Erb, G. Palumbo and J.A. Szpunar, *J. Magn. Magn. Mater*. 187(1998)325
41. F. Czerwinski and Z. Kedzierski, *J. Mater. Sci.* 32(1997)2957
42. J.M. Williams, H.J. Blythe and V.M. Fedosyuk, *J. Magn. Magn. Mater*. 155(1996) 355
43. R.L. Whetten, D.M. Cox, D.J. Trevor and A. Kaldor, *Phys. Rev. Lett*. 54(1985)1494
44. G.K. Boschloo, A. Goossens and J. Schoonman, *J. Electroanal. Chem*. 428(1997) 25
45. A. Durant, J.-L. Delplancke, R. Winand and J. Reisse, *Tetrahedron Letters* 36(1995) 4257
46. R.R. Adzic, J. Wang and B.M. Ocko, *Electrochim. Acta* 40(1995) 83
47. M.J. Aus, B. Szpunar, U. Erb, A.M. El-Sherik, G. Palumbo and K.T. Aust, *J. Appl. Phys*. 75(1994)3632
48. C.H. Seah, S. Mridha and L.H. Chan, *J. Materials Processing Technology* 89-90 (1999) 432
49. U. Dehlinger and F. Giesen, *Z. Metallkunde* 24(1932)197
50. E. Raub and A. Engel, *Z. Metallkunde* 41(1950) 485
51. A. Robertson, U. Erb and G. Palumbo, *NanoStructured Materials* 12(1999)1035
52. T.R. Haasz, K.T. Aust, G. Palumbo, A.M. El-Sherik and U. Erb, *Scripta Metall. et Mater*. 32 (1995)423
53. G. Palumbo, S.J. Thorpe and K.T. Aust, *Scripta Metall. et Mater*. 24(1990)1347
54. U. Erb, G. Palumbo, B. Szpunar and K.T. Aust, *NanoStructured Materials* 9(1997) 261
55. H. Natter, M. Schmelzer and R. Hempelmann, *J. Mater. Res*. 13(1998) 1186
56. H. Natter, M. Schmelzer, M.-S. Löffler, C.E. Krill, A. Fitch and R. Hempelmann, *J. Phys. Chem.* B104(2000)2467
57. J. Reisse, H. François, J. Vandercammen, O. Fabre, A. Kirsch-De Mesmaeker, C. Maerschalk and J.L. Delplancke, *Electrochim. Acta* 39(1994) 37

58. D. van Heerden, E. Zolotoyabko and D. Shechtman, *J. Mater. Res*. 11(1996) 2825
59. F. Ebrahimi, Q. Zhai and D. Kong, *Mater. Sci. and Eng*. A255(1998)20
60. F. Czerwinski, *Electrochim. Acta* 44(1998) 667
61. I. Brooks and U. Erb, *Scripta Mater*. 44(2001)853
62. P.L. Cavallotti, B. Bozzini, L. Nobili and G. Zangari, *Electrochim. Acta,*39(1994) 1123
63. B. Bozzini, P.L. Cavallotti and G. Giovannelli, *Metal Finishing* 100(4) (2002) 50
64. B. Bozzini, P.L: Cavallotti, J.-P. Celis and A. Fanigliulo, "Anodic behaviour of amorphous NiP/tin multilayers in an acidic chloride solution" *Corros. Sci.,* in press
65. D.M. Tench and J.T. White, *J. Mater. Sci*. 27(1992)5286
66. D. Aimawlawi, N. Coombs and M. Moskovits*, J. Appl. Phys*. 70(1991)4421
67. B. Bozzini, *J. Mater. Sci. Lett*. 20(2001) 867
68. T.J. Lee, K.G. Sheppard, A. Ganburg and L. Klein, Electrochemical Microfabrication II, M. Datta, K. Sheppard, J. Dukovic ed.s, The Electrochemical Society, Pennington N.J. (1994), Proc. Vol. 94-2, p. 231.
69. C.R. Martin, *Science* 266(1994) 1961
70. A. Kazadi Mukenza Bantu, J. Rivas, G. Zaragoza, M.A. López-Quitela and M.C. Blanco, *J. Non-Cryst. Solids* 287(2001)5
71. S. Valizadeh, J.M. George, P. Leisner and L. Hultman, *Electrochim. Acta* 47(2001)865
72. M. Nishizawa, V.P. Menon and C.R. Martin, *Science* 268(1995)700
73. J.L. Delplancke, M. Sun, T.J. O'Keefe and R. Winand, *Hydrometallurgy* 24(1990)179
74. I. Bakonyi, E. Tóth-Kádár, L. Pogány, A. Cziráki, I. Geröcs, K. Varga-Josepovits, B. Arnold and K. Wetzig, *Surf. and Coat. Technol*. 78(1996) 124
75. M. Ye, J.L. Delplancke, G. Berton, L. Segers and R. Winand, *Surf. and Coat. Technol*. 105(1998) 184
76. E. Budevski, G. Staikov and W.J. Lorenz, Electrochemical Phase Formation and Growth - An Introduction to the Initial Stages of Metal Deposition, Wiley-VCH, Weinheim-D (1996)
77. R.T. Pötzschke, C.A. Gervasi, S. Vinzelberg, G. Staikov and W.J. Lorenz, *Electrochim. Acta* 40(1995)1469
78. P. Van den Brande and R. Winand, *Surf. and Coat. Technol*. 52(1992) 1
79. P. Van den Brande and R. Winand, *J. Appl. Electrochem*. 23(1993)1089
80. D.M. Kolb, in: Advances in Electrochemistry and Electrochemical Engineering, H. Gerischer, C.W. Tobias ed.s, Wiley, N.Y. (1978), Vol. 11, p. 125.
81. A. Aramata, in: Modern Aspects of Electrochemistry, J.O'M. Bockris, B.E. Conway, ed.s, Plenum Press, NY (1997), Vol. 31
82. R. Kaishew and B. Mutaftschiew, *Electrochim. Acta* 10(1965) 643
83. I. Markov, *Thin Solid F*ilms 35, 11 (1967) and 35(1967)21
84. R. Winand, *Hydrometallurgy* 29(1992) 567
85. H. Natter and R. Hempelmann, *J. Phys. Chem*. 100(1996)19525
86. J.L. Delplancke, M. Sun, T.J. O'Keefe and R. Winand, *Hydrometallurgy* 23(1989)47
87. R. Winand, *Electrochim. Acta* 43, 2925 (1998)
88. M.Y. Abyaneh, M. Fleischmann and M. Labram, Electrocrystallization, R. Weil, R.G. Barradas ed.s, The Electrochemical Society, Pennington NJ (1981), Proc. Vol. 81-6, p. 1
89. V. Tsakova and A. Michev, *J. Electroanal. Chem*. 235(1987) 249
90. T. Vargas and R. Varma, in: Techniques for Characterization of Electrodes and Electrochemical Processes, R. Varma, J.R. Selamn ed.s, John Wiley & Sons, N.Y. (1991), p. 717.
91. G. Hills, A.K. Pour and B. Schafriker, *Electrochim. Acta* 28(1983)891
92. G. Gunawardena, G. Hills and I. Montenegro, *J. Electroanal. Chem*. 138(1982)241
93. M. Fleischmann, C. Gabrielli, M. Labram and A. Sattar, *Surf. Sci*. 101(1980) 583
94. F. Czerwinski and J.A. Szpunar, *NanoStructured Materials* 11(1999)669
95. F. Möller, O.M. Magnussen and R.J. Behm, *Phys. Rev. Lett*. 77(1996)3165

96. O.M. Magnussen, F. Möller, M.R. Vogt and R.J. Behm, in: Electrochemical Nanotechnology, W.J. Lorenz and W. Plieth ed.s, Wiley-VCH, Weinheim (D) (1998) p.159
97. B. Bozzini, G. Giovannelli, S. Natali, A. Fanigliulo and P.L. Cavallotti, *J. Mater. Sci*. 37(2002)3903
98. B. Bozzini, G. Giovannelli, S. Natali, M. Serra and A. Fanigliulo, *J. Appl. Elect*rochem. 32 (2002)165
99. B. Bozzini and A. Fanigliulo, *J. Crystal Growth* 243(2002) 190
100. D. Carnal, P.I. Oden, U. Müller, E. Schmidt and H. Siegenthaler, *Electrochim. Acta* 40(1995)1223
101. U. Schmidt, S. Vinzelberg and G. Staikov, *Surf. Sci*. 348 (1996) 261
102. H. Siegenthaler, K. Jüttner, E. Schmidt and W.J. Lorenz, *Electrochim. Acta* 23(1978) 1009
103. R.J. Nichols, W. Beckmann, H. Meyer, N. Batina and D.M. Kolb, *J. Electroanal. Chem*. 330(1992)381
104. D.M. Kolb, *Surf. Sci.* 500(2002) 722
105. M. Wünsche, R.J. Nichols, R. Schumacher, W. Beckmann and H. Meyer, *Electrochim. Acta* 38(1993)647
106. X.G. Zhang and U. Stimming, *J. Electroanal. Chem*. 291(1990) 273
107. J.R. LaGraaf and A.A. Gewirth, *J. Phys. Chem*. 98(1994)11246
108. J.R. LaGraaf and A.A. Gewirth, *J. Phys. Chem*. 99(1995) 10009
109. W. Obretenov, U. Schmidt, W.J. Lorenz, G. Staikov, E. Budevski, D. Carnal, U. Müller, H. Siegenthaler and E. Schmidt, J. *Electrochem. Soc.* 140(1993) 692
110. S.G. Garcia, D. Salinas, C. Mayer, J.R. Vilche, H.-J. Pauling, S. Vinzrlberg, G. Staikov and W.J. Lorenz, *Surf. Sci*. 316(1994) 143
111. M.J. Esplandiu, M.A. Schneeweiss and D.M. Kolb, *Phys. Chem. Chem. Phys*. 1(1999)4847
112. M.S. Zei, G. Qiao, G. Lehmpfuhl and D.M. Kolb, Ber. Ber. Bunsenges. *Phys. Chem*. 91(1987)349
113. O.M. Magnussen, J. Hotlos, R.J. Nichols, D.M. Kolb and R.J. Behm, *Phys. Rev. Lett*. 64(1990) 2929
114. T. Hachiya, H. Honbo and K. Itaya, *J. Electroanal. Chem*. 315(1991) 275
115. Z. Shi and J. Lipkowski, *J. Electroanal. Chem*. 365(1994) 303
116. M.F. Toney, J.N. Howard, J. Richer, G.L. Borges, J.G. Gordon and O.R. Melroy, *Phys. Rev. Lett*. 75 (1995)4472
117. K. Sashikata, N. Furuya and K. Itaya, *J. Electroanal. Chem*. 316(1991)361
118. N. Kimizuka and K. Itaya, *Fadaray. Discuss*. 91(1992) 117
119. C.-H. Chen, S.M. Vesecky and A.A. Gewirth, *J. Am. Chem. Soc*. 114(1992)451
120. J. Hotlos, O.M. Magnussen and R.J. Behm, *Surf. Sci*. 335(1995) 129
121. F. Möller, O.M. Magnussen and R.J. Behm, *Phys. Rev*. B51(1995)2484
122. F. Möller, O.M. Magnussen and R.J. Behm, *Electrochim. Acta* 40(1995)1259
123. S. Sugita, T. Abe and K. Itaya, *J. Phys. Chem*. 97(1993) 8780
124. D. Barkey, F. Oberholzer and Q. Wu, *Phys. Rev. Lett*. 75(1995) 2980
125. N. Shinotsuka, K. Sashikata and K. Itaya, *Surf. Sci*. 335(1995)75
126. C.-H. Chen and A.A. Gewirth, *J. Am. Chem. Soc*. 114(1992) 5439
127. B.K. Niece and A.A. Gewirth, *Langmuir* 12(1996) 4909
128. H. Siegenthaler and K. Jüttner, *Electrochim. Acta* 24(1979) 109
129. A. Popov, N. Dimitrov, D. Kashchiev, T. Vitanov and E. Budevski, *Electrochim. Acta* 38(1992)2173
130. J.W. Schultze, F.D. Koppitz and M.M. Lohrengel, Ber. Ber. Bunsenges. *Phys. Chem*. 78(1974)693
131. J.E.T. Andersen and P. Møller, *J. Electrochem. Soc.* 142(1995)2225
132. J.A. Meyer, I.D. Baikie, E. Kopatzki and R.J. Behm, *Surf. Sci*. 365(1996)L647

133. G. Andreasen, M. Nazzaro, J. Ramirez, R.C. Salvarezza and A.J. Arvia, *J. Electrochem. Soc*. 143(1996) 466
134. L.H. Jenkins, *J. Electrochem. Soc*. 117(1970) 630
135. (a) N.A. Pangarov and S.D. Vitkova, *Electrochim. Acta* 11, 1719 (1966). (b) N.A. Pangarov, S.D. Vitkova and I. Uzunova, *Electrochim. Acta* 11, 1747 (1966). (c) N.A. Pangarov and V. Velinov, *Electrochim. Acta* 11, 1753 (1966)
136. K.I. Popov, S.S. Djokic and B.N. Grgur, Fundamental Aspects of Electrometallurgy, Kluwer N.Y. (2002) Chapters 3 and 5.
137. T. Erdey-Gruz and Z. Volmer, *Z. Phys. Chem*. 157A(1931) 165
138. M. Fleischmann and H.R. Thirsk, *Electrochim. Acta* 1(1959) 146
139. K.I. Popov, N.V. Krstajic and S.R. Popov, *Surf. Technol*. 20(1983)203
140. A.T. Dimitrov, S. Hadzi-Jordanov, K.I. Popov, M.G. Pavlovic and V. Radmilovic, *J. Appl. Electrochem*. 28(1998)791
141. K.I. Popov, M.G. Pavlovic, B.N. Grgur, A.T. Dimitrov and S. Hadzi-Jordanov, *J. Appl. Electrochem*. 28(1998) 797
142. V. Radmilovic, K.I. Popov, M.G. Pavlovic, A.T. Dimitrov and S. Hadzi-Jordanov, *J. Solid State Electrochem*. 2(1998)162
143. S. Meibuhr, E. Yeger, A. Kozawa and F. Hovorka, *J. Electrochem. Soc*. 110(1963) 190
144. K.I. Popov, N.V. Krstajic and S.R. Popov, *Surf. Technol*. 20(1983)199
145. K.I. Popov, Z.P. Rodaljevic, N.V. Krstajic and S.D. Novakovic, *Surf. Technol*. 25(1985) 217
146. I. Bakonyi, E. Tóth-Kádár, L. Pogány and A. Cziráki, *Surf. and Coat. Technol*. 78(1996) 124
147. A.M. Alfantazi, G. Brehaut and U. Erb, *Surf. and Coat. Technol*. 89(1997)239
148. A. Milchev, W.S. Kruijt, M. Sluyters-Rehbach and J.H. Sluyters, *J. Electroanal. Chem*. 362(1994) 21
149. W.S. Kruijt, M. Sluyters-Rehbach, J.H. Sluyters and A. Milchev, *J. Electroanal. Chem*. 371(1993)13
150. A.R. Despic and T.Lj. Trisovic*, J. Appl. Electrochem*. 23(1992)662
151. U. Cochen, F.B. Koch and R. Sard*, J. Electrochem. Soc*. 130(1983)1987
152. L.H. Bennett, D.S. Lashomore, M.P. Dariel, M.J. Kaufman, M. Rubinstein, P. Lubitz, O. Zodak and J. Yahalom*, J. Magn. Magn. Mater*. 67(1987) 239
153. J. Yahalom and O. Zadoc*, J. Mater. Sci*. 22(1987) 499
154. D.S. Lashmore and M.P. Dariel, *J. Electrochem. Soc*. 135(1988)1218
155. A.R. Despic, V.D. Jovic and S. Spaic*, J. Electrochem. Soc*. 134(1989)1651
156. D.M. Tench and J.T. White, *J. Electrochem. Soc*. 137(1990) 3061
157. D. Simunovich, M. Schlesinger and D.D. Snyder, *J. Electrochem. Soc*. 141(1994)L10
158. T.P Moffat, *J. Electrochem. Soc*. 142(1995)159
159. R.R. Oberle and R.C. Cammarata, *Scripta Metall. et Mater*. 32(1995) 583
160. D.M. Tench and J.T. White*, J. Electrochem. Soc*. 139(1992)443
161. Y. Jyoko, S. Kashiwabara and Y. Hayashi*, J. Magn. Magn. Mater*. 156(1996)35
162. L.M. Goldman, B. Blancpain and F. Spaepen, *J. Appl. Phys*. 60(1986) 1374
163. C.A. Ross, L.M. Goldman and F. Spaepen, *J. Electrochem. Soc*. 140(1993)91
164. C.N. Panagopoulos, V.D. Papachristos, U. Wahlstrom, P. Leisner and L.W. Christoffersen, *Scripta Mater*. 43(2000)677
165. J.L. Delplancke, M. Ongaro and R. Winand, *J. Appl. Electrochem*. 22(1992)843
166. G. Poli and L. Peraldo Bicelli, *Met. Ital*. 54(1962) 497
167. K. Subramanian and S. Nageswar, *Surface Technol*. 10(1980)7
168. L. Peraldo Bicelli and G. Poli, *Electrochim. Acta* 11(1966)289
169. V.M. Kozlov and L. Peraldo Bicelli, *J. Crystal Growth* 165(1996)421
170. V.M. Kozlov and L. Peraldo Bicelli, *J. Crystal Growth* 177(1997) 289
171. V.M. Kozlov, L. Peraldo Bicelli and V.N. Timoshenko, *J. Crystal Growth* 183(1998)456

172. R.J. Nichols, D.M. Kolb and R.J. Behm*, J. Electroanal. Chem*. 313(1991)109
173. J.E.T. Andersen, G. Bech-Nielsen and P. Møller*, Surf. and Coat. Technol*. 70(1994)87
174. J.E.T. Andersen, G. Bech-Nielsen and P. Møller, *Surf. and Coat. Technol*. 67(1994)151
175. J.E.T. Andersen, G. Bech-Nielsen, P. Møller and J.C. Reeve, *J. Appl. Electrochem*. 26(1996)161
176. N. Breuer, A.M. Funtikov, U. Stimming and R. Vogel, *Surf. Sci*. 335(1995)145
177. N. Breuer, U. Stimming and R. Vogel, *Electrochim. Acta* 40(1995)1401
178. T.P. Moffat, in: Electrochemical Nanotechnology, W.J. Lorenz and W. Plieth ed.s, Wiley-VCH, Weinheim (D) (1998) p. 171
179. G.M. Brisard, E. Zenati, H.A. Gasteiger, N.M. Markovic and P.N. Ross, *Langmuir* 11(1995) 2221
180. W.U. Schmidt, R.C. Alkire and A.A. Gewirth, *J. Electrochem. Soc*. 143(1996) 3122
181. A. Damjanovic, *Plating* 52(1965) 1017
182. K.I. Popov, M.G. Pavlovic, Lj.J. Pavolovic, M.I. Cekerevac and G.Z. Removic, *Surf. and Coat. Technol*. 34(1988)355
183. C.A. Schuh, T.G. Nieh and T. Yanasaki, *Scripta Mater*. 46(2002)735
184. A. Despic and K. Popov, in: Modern Aspects of Electrochemistry, B.E. Conway, J.O'M. Bockris eds., Plenum Press, NY (1972) Vol. 7
185. R.J. Nichols, C.E. Bach and H. Meyer, Ber. Ber. Bunsenges. *Phys. Chem*. 97(1993) 1012
186. K.I. Popov, B.N. Grgur, M.G. Pavlovic and V. Radmilovic, *J. Serb. Chem. Soc*. 58(1993)1055
187. F. Czerwinski, *NanoStructured Materials* 10(1998)1363
188. B. Bozzini, E. Griskonis, A. Fanigliulo and A. Sulcius, *Surf. and Coat. Technol*. 154(2002)294
189. A.M. El-Sherik and U. Erb, *J. Mater. Sci*. 30(1995)5743
190. F.Czerwinski, J.A. Szpunar and W.W. Smelzer, *Metall. Mater. Trans*. A27(1996)3649
191. L. Graf and W. Weser, *Electrochim. Acta* 2(1960)145
192. S. Kang, J.-S. Yang and D.N. Lee, *Plat. and Surf. Fin*. 82(10) (1995)67
193. C. Lizzul Rinne, J.J. Hren and P.S. Fewdik*, J. Electrochem. Soc*. 149(2002)C150
194. B. Bozzini, A. Fanigliulo and M. Serra*, J. Crystal Growth* 231(2001)589
195. B. Bozzini, D. Picenoni and A. Fanigliulo, "Observation of Pentagonal Crystallites in Electrodeposited Gold and Copper", Praktische Metallographie / *Practical Metallography*, in press
196. J.W. Diggle, A.R. Despic and J.O'M. Bockris, *J. Electrochem. Soc*. 116(1969)1503
197. K.I. Popov and M.I. Cekerevac, *Surf. Technol*. 37(1989)435
198. K. Popov, N. Krstajic and M. Cekerevac, in: Modern Aspects of Electrochemistry, R.E. White, B.E. Conway, J.O'M. Bockris ed.s, Plenum Press, N.Y. 1996, Vol. 30
199. K. Popov and M. Pavlovic, in: Modern Aspects of Electrochemistry, R.E. White, B.E. Conway, J.O'M. Bockris ed.s, Plenum Press, N.Y. (1993), Vol. 24
200. N. Ibl, in: Advances in Electrochemistry and Electrochemical Engineering, P. Delahay, C.W. Tobias ed.s, Interscience, N.Y. (1962), Vol. 2, p. 12
201. K.I. Popov, M.G. Pavlovic and M.D. Maksimovic*, J. Appl. Electrochem*. 12(1982) 525
202. M.G. Pavlovic, S. Kindlova and I. Rousa,. *Electrochim. Acta* 37(1992)23
203. K.I. Popov, M.G. Pavolovic, M.D. Maksimovic and S.S. Krstjic*, J. Appl. Electrochem*. 8 (1978)503
204. J.L. Delplancke, O. Bouesnard, J. Reisse and R. Winand, Mater. Res. Soc. Symp. Proc. 451(1997)383
205. K.I. Popov and N.V. Krstajic, *J. Appl. Electrochem*. 13(1983)775
206. M.M. Jaksic, *Surf. Technol*. 24(1985)193
207. A.L. Barabasi and H.E. Stanley, Fractal Concepts in Growth Phenomena, Cambridge University Press, Cambridge (1995).
208. G. Marshall and P. Mocskos, *Phys. Rev*. E 55(1997)549
209. F. Family and T. Vicsek ed.s, Dynamics of Fractal Surfaces, World Scientific, Singapore (1991)
210. R.C. Salvarezza and A.J. Arvia, in: Modern Aspects of Electrochemistry, B.E. Conway, J.O'M. Bockris ed.s, Plenum Press, NY (1995), Vol. 28

211. S.R. Forrest and T.A. Witten jr., *J. Phys*. A12(1979)L109
212. S. Bandyopadhyay, S. Roy and D. Chakravorty, *Solid State Comm*. 99(1996) 835
213. H. Natter, T. Krajewski and R. Hempelmann, Ber. Ber. Bunsenges. *Phys. Chem*. 100(1996) 55
214. N. Ibl, J.A. Puippe and H. Angerer, *Surf. Technol*. 6(1978) 287
215. K. Popov and M. Miodrag, in: Modern Aspects of Electrochemistry, R.E. White, B.E. Conway, J.O'M. Bockris ed.s, Plenum Press, N.Y. (1989), Vol. 19
216. S.K. Ghosh, A.K. Grover, G.K. Dey and M.K. Totlani. *Surf. and Coat. Technol*. 126(2000)48
217. M.G. Pavlovic, M.D. Maksimovic, K.I. Popov and M.B. Krsul, *J. Appl. Electrochem*. 8(1978) 61
218. K.I. Popov, M.D. Maksimovic, M.G. Pavolovic and G.R. Ostojic, *J. Appl. Electrochem*. 7(1977)331
219. K.I. Popov, M.D. Maksimovic and D.C. Totovski, *Surf. Technol*. 17(1982) 125
220. A.M. El-Sharik, U. Erb, G. Palumbo and K.T. Aust, *Scripta Metall. et Mater*. 27(1992)1185
221. U. Erb, *NanoStructured Materials* 6(1995)533
222. A. Cerezo, M. Abraham, P. Clifton, H. Lane, D.J. Larson, A.K. Petford-Long, M. Thuvander, P.J. Warren and G.D.W. Smith, *Micron* 32(2001) 731
223. M. Cherkaoui, E. Chassaing and K.V. Quang, *Surf. and Coat. Technol*. 34(1988)243
224. R.T. Choo, J.M. Toguri, A.M. El-Sherik and U. Erb, *J. Appl. Electrochem*. 25(1995) 384
225. T. Yamasaki, P. Schloßmacher, K. Ehrlich and Y. Ogino, *NanoStructured Materials* 10(1998)375
226. B. Bozzini and A. Fanigliulo, *Trans. Inst. Metal* Fin. 80(2002)25
227. D.-Y. Park, N.V. Myung, M. Schwartz and K. Nobe, *Electrochim. Acta* 47(2002)2893
228. T. Yamasaki, *Scripta Mater*. 44(2001)1497
229. A.M. Alfantazi and U. Erb, *Mater. Sci. and Eng*. A212(1996)123
230. A.F. Zimmermann, D.G. Clark, K.T. Aust and U. Erb, *Materials Letters* 52(2002) 85
231. G.D. Hibbard, J.L. McCrea, G. Palumbo, K.T. Aust and U. Erb, *Scripta Mater*. 47(2002) 83
232. H. Wang, S. Yao and S. Matsumura, *Surf. and Coat. Technol*. 157(2002)166
233. B. Bozzini, *Trans. Inst. Metal. Fin*. 78(2000) 93
234. G. Hibbard, K.T. Aust, G. Palumbo and U. Erb, *Scripta Mater.* 44(2001)513
235. T. Nasu, M. Sakurai, T. Kamiyama, T. Usuki, O. Uemura and T. Yamasaki, *J. Non-Cryst. Solids* 312-314(2002) 319
236. Kh. Saber, C.C. Koch and P.S. Fedkiw, *Mater. Sci. and Eng*. A341(2003) 174
237. F. Della Torre, H. Van Swygenhoven and M. Victoria, *Acta Mater*. 50(2002)3957
238. F. Czerwinski, H. Li, F. Megret, J.A. Szpunar, D.G. Clark and U. Erb, *Scripta Mater*. 37(1997)1967
239. A.F. Zimmermann, G. Palumbo, K.T. Aust and U. Erb, *Mater. Sci. and Eng*. A328(2002)137
240. M. Abraham, P. Holdway, M. Thuvander, A. Cerezo and G.D.W. Smith, *Surf. Eng*. 18(2002)151
241. B. Bozzini and P.L. Cavallotti, Proc. 197th ECS Meeting, Toronto, Canada, 14-18/05/2000, Hydrogen at Surfaces and Interfaces, G. Jerkiewicz, J.M. Feliu, B.N. Popov ed.s, Electrochemical Society Proceedings, Pennington NJ (2000), Vol. 16, p. 174.
242. H. Wolf, Z. Guan, X. Li and Th. Wichert, *Hyperfine Interactions* 136/137(2001) 281
243. R. Winand, Ph. Van Ham, R. Colin and D. Milojevic, *J. Electrochem. Soc*. 144(1997) 436
244. B. Bozzini and P.L. Cavallotti, Praktische Metallographie - *Practical Metallography*, 38(2001)88
245. B. Bozzini, G. Giovannelli, S. Natali, B. Brevaglieri, P.L. Cavallotti and G. Signorelli, *Engineering Failure Analysis* 6(1998) 83
246. Electrochemical Nanotechnology. W.J. Lorenz, W. Plieth ed.s. Wiley-VCH, Weinheim (1998).
247. B. Bozzini and P.L. Cavallotti, *J. Electrochem. Soc*. 148(2001) C231
248. T. Turi and U. Erb, *Mater. Sci. and Eng*. A204(1995)34
249. A. Michels, J. Weissmüller, U. Erb and J.G. Barker, *Phys. Status Solidi* A189(2002)509
250. B. Bozzini, G. Giovannelli and S. Natali, *Scripta Mater*. 43(2000)877
251. S.K. Ghosh, A.K. Grover and M.K. Totlani, *Trans. Inst. Metal Fin*. 80(2002)56

252. G. Zangari, B. Bozzini, P.L. Cavallotti, G. Fontana, P.G. Maisto and E. Terrenzio, *J. Magn. Magn. Mater*. 133(1994)511
253. A. Fanigliulo and B. Bozzini, *J. Electroanal. Chem*. 530(2002)53
254. B. Bozzini and A. Fanigliulo, "An in-situ spectroelectrochemical Raman investigation of Au electrodeposition and electrodissolution in $KAu(CN)_2$ solution" *J. Appl. Electrochem*., in press
255. N. Wang, Z. Wang, K.T. Aust and U. Erb, *Mater. Sci. and Eng*. A237(1997) 150
256. D.L. Wang, Q.P. Kong and J.P. Shui, *Scripta Metall. et Mater*. 31(1994)47
257. Y.B. Park, S.-H. Hong, C.S. Ha, H.Y. Lee and T.H. Yim, Mater. *Sci. Forum* 408-412(2002) 931
258. D.H. Jeong, U. Erb, K. Aust and G. Palumbo, Mater. *Sci. Forum* 408-412(2002)925
259. A.M. El-Sherik and U. Erb, in: Proc. of Nickel-Cobalt 97, F.N. Alpas Ed., Canadian Institute for Minerals, Metals and Petroleum, Montreal (1997), Vol. 4, p. 257
260. B. Bozzini, C. Martini, A. Fanigliulo and F. Bogani, "A tribological study of electrodeposited Au-Cu-Cd", *Metal Finishing*, in press
261. B. Bozzini, M. Serra and A. Fanigliulo, *Trans. Inst. Metal Fin*. 79(2001) 133
262. B. Bozzini, P.L. Cavallotti and G. Giovannelli, *Proc. Royal Microscopical Society* 31(1) (1996)41
263. B. Bozzini and P.L. Cavallotti*, J. Appl. Electrochem*. 31(2001)897
264. B. Bozzini and P.L. Cavallotti, *Trans. Inst. Matal Fin*. 78(2000) 227
265. I. Bakonyi, L.K. Varga, A. Lovas, E. Toth-Kadar and A. Solyom*, J. Magn. Magn. Mater*. 50(1985) 111
266. H.J. Blythe and V.M. Fedosyuk, *Phys. Status Solidi* A146(1994) K13
267. B. Bozzini, G. Zangari and P.L. Cavallotti, *Electrochim. Acta* 39(1994) 1787
268. B. Bozzini, P.L. Cavallotti, A. Martelli, G. Zangari and Ch.J. Raub, in: Edelmetalle - Moderne Technologien und Anwendungen, A. Choms, E. Schrode ed.s, Eugen G. Leuze Vlg., Saulgau/Württ. (D) (1992), p. 50.
269. B. Bozzini, D. De Vita, A. Sportoletti, G. Zangari, P.L. Cavallotti and E. Terrenzio, *J. Magn. Magn. Mater*. 120(1993) 300
270. B Bozzini, G. Zangari and P.L. Cavallotti, in: Magnetic Properties of Matter, G. Asti, D. Fiorani, F. Lucari ed.s, World Scientific, Singapore (1991), p. 521
271. J. Dille, J.L. Delplancke, J. Charlier and R. Winand, *Mater. Res. Soc. Symp. Proc*. 362(1995)231
272. D.N. Lee, S. Kang and J. Yang, *Plat. and Surf. Fin.* 5(1995)76
273. Y.B. Park, J. Park, C.S. Ha and T. Yim, *Mater. Sci. Forum* 408-412(2002)919
274. H. Li, F. Czerwinski and J.A. Szpunar, *NanoStructured Materials* 9(1997) 673
275. A.M. El-Sherik, U. Erb and J. Page, *Surf. and Coat. Technol*. 88(1997)70
276. G.D. Hughes, S.D. Smith, C.S. Pande, H.R. Johnson and R.W. Armstrong, *Scripta Metall*. 20(1986) 93
277. R.R. Oberle, M.R. Scanlon, R.C. Cammarata and P.C. Serasons, *Appl. Phys. Lett*. 66(1995) 19
278. R. Rofagha, R. Langer, A.M. El-Sherik, U. Erb, G. Palumbo and K.T. Aust, *Scripta Metall. et Mater.* 25(1991) 2867
279. B. Bozzini, C. Lenardi, M. Serra and A. Fanigliulo, *British Corrosion Journal* 37(2002)173
280. B.E. Jacobson and J.W. Sliwa, *Plat. and Surf. Fin*. 9(1979) 42
281. G. Palumbo, D.M. Doyle, A.M. El-Sherik, U. Erb and K.T. Aust, *Scripta Metall. et Mater.* 25(1991)679
282. D.M. Doyle, G. Palumbo, K.T. Aust, A.M. El-Sherik and U. Erb, *Acta Metall. et Mater.* 43(1995)3027
283. C. Cheung, G. Palumbo and U. Erb, *Mater. Sci. and Eng*. A185(1994)39
284. C. Cheung, F. Djuanda, U. Erb and G. Palumbo, *Scripta Metall. et Mater*. 31(1994) 735
285. M. Boniardi, G.C. Martinelli, B. Bozzini and R. Vitali, *International Journal of Materials and Product Technology* 15(2000) 63

286. G. Palumbo, F. Gonzales, A.M. Brennenstuhl, U. Erb, W. Shmayada and P.C. Lichtenberger, *NanoStructured Materials* 9(1997)737
287. D. Clark, D. Wood and U. Erb, *NanoStructured Materials* 9(1997)755
288. T. Hentschel, D. Isheim, R. Kirchheim, F. Müller and H. Kreye, *Acta Mater*. 48(2000)933
289. H. Cesiulis, A. Baltutiene, M. Donten, M.L. Donten and Z. Stojek*, J. Solid State Electrochem*. 6(2002)237
290. B. Bozzini, G. Bollini, F. Pavan and P.L. Cavallotti, *Trans. Inst. Metal Fin*. 75(1997)175
291. B. Bozzini, F. Pavan and P.L. Cavallotti, *Trans. Inst. Metal Fin*. 76(1998)171
292. B. Bozzini, E. Griskonis, A. Sulcius and P.L. Cavallotti, *Plat. and Surf. Fin*. 88(2001) 64
293. B. Bozzini and M. Boniardi, *J. Mater. Sci*. 36(2001)511
294. B. Bozzini, F. Pavan, V. Accardi and P.L. Cavallotti, *Metal Finishing* 97(5) (1999)33
295. A.M. Alfantazi and U. Erb, *J. Mater. Sci. Lett*. 15(1996)1361
296. A.M. Alfantazi and U. Erb, *Corrosion* 52(1996)880
297. B. Reents and W. Plieth, in: Electrochemical Nanotechnology, W.J. Lorenz and W. Plieth ed.s, Wiley-VCH, Weinheim (D) (1998) p.277
298. B. Bozzini, A. Fanigliulo, G. Giovannelli, S. Natali and C. Mele, "Electrodeposition of Au-Sn alloys from acid Au(III) baths", accepted for publication in: *J. Appl. Electrochem.*
299. A. Fanigliulo and B. Bozzini, *Electrochim. Acta* 47(2002)4511
300. M. Tadjeddine and J.P. Flamant, *Chem. Phys*. 240(1999)39
301. B. Bozzini, P.L. Cavallotti, G. Giovannelli and S. Natali. Proc. 197th ECS Meeting, Toronto, Canada, 14-18/05/2000, "Hydrogen at Surfaces and Interfaces", G. Jerkiewicz, J.M. Feliu, B.N. Popov ed.s, PV 2000-16 Electrochemical Society Proceedings, p. 242.
302. B. Bozzini, G. Giovannelli, C. Lenardi, M. Serra and M. Placidi. "Effects of Organic Additives on Morphological Evolution of Electrodeposited Au and Au Alloys" 199th Electrochemical Society Meeting, 25-29/03/2001 Washington D.C. Proc. In press.
303. T. Iwasita and F. C. Nart. In “Advances in Electrochemical Science and Engineering”. H. Gerischer and C. W. Tobias ed.s. Wiley-VCH, Weinheim (D) (1995) p. 123